



Science Arts & Métiers (SAM)

is an open access repository that collects the work of Arts et Métiers Institute of Technology researchers and makes it freely available over the web where possible.

This is an author-deposited version published in: <https://sam.ensam.eu>
Handle ID: [.http://hdl.handle.net/10985/25609](http://hdl.handle.net/10985/25609)

To cite this version :


Giuseppe SCIUMÈ, Murilo Henrique MOREIRA, Stefano DAL PONT - Thermo-hygro-chemical model of concrete: from curing to high temperature behavior - Materials and structures - Vol. 57, n°8, - 2024

Any correspondence concerning this service should be sent to the repository

Administrator : scienceouverte@ensam.eu



Thermo-hygro-chemical model of concrete: from curing to high temperature behavior


Giuseppe Sciumè · Murilo Henrique Moreira · Stefano Dal Pont 

Abstract Concrete is a heterogeneous multiphase material composed of various solid phases that interact both physically and chemically with each other and with the water filling the pores. Among these solid phases, a crucial role is played by the calcium silicate hydrates (C–S–H), which are the primary products of cement hydration and are primarily responsible for the material's physical properties. When concrete is subjected to high temperatures, the chemically bound water in C–S–H is progressively released, leading to a degradation in the strength and durability properties of the concrete. Hence, understanding how the dynamics of C–S–H dehydration and the corresponding evolution of hygro-mechanical properties (e.g. strength, permeability, porosity) are related with the characteristic observed phenomenology of spalling is crucial to assess the resistance of

a structure under high temperature. Within this context, multiphysics thermo-hygro-chemical (THC) numerical models now play a pivotal role in predicting and analyzing structures' performance under fire accidents. However, to enhance the reliability of numerical results, properly accounting for the initial hygro-chemical state of the structure just before the accident is of chief importance. This work presents a monolithic fully-coupled unified THC mathematical model enabling the simulation of the full service life of the material: from casting (early-age behavior and curing), through aging, until the eventual occurrence of an accident (high temperature, high pressure, ...). The model provides the evolution of the hydration reaction as a function of time, temperature, and relative humidity, as well as the eventual dehydration occurring at high temperature. The main contribution of this work lies in the proposition of general chemophysical constitutive relationships that incorporate the influence of the hygro-thermal state of the material as well as that of C-S-H hydration/dehydration in a fully-coupled manner. The evolution of volume fraction of phases and porosity during hydration/dehydration follows Powers' stoichiometric model, while a novel adsorption–desorption model is proposed to properly account for the irreversibility of chemical damage in the porous microstructure. This enables an alternative, simpler approach requiring only a limited number of experiments for the model calibration. The model is firstly benchmarked by simulating the early-age behavior of a concrete sample, and it is then

G. Sciumè
Arts et Metiers Institute of Technology, CNRS, University of Bordeaux, Bordeaux INP, INRAE, I2M Bordeaux, Avenue d'Aquitaine, 33607 Pessac, France

M. H. Moreira
Federal University of Sao Carlos, Graduate Program in Materials Science and Engineering (PPGCEM), Rod. Washington Luiz, km 235, São Carlos, SP 13565-905, Brazil

S. Dal Pont 
Université Grenoble Alpes, CNRS, Grenoble INP, 3SR, 38000 Grenoble, France
e-mail: stefano.dalpont@univ-grenoble-alpes.fr

validated against experimental results of temperature, gas pressure and mass loss under heating. Our results highlight a non-negligible impact of the initial (which in real cases is usually heterogeneous) hygral state on the predicted behavior at high temperature and unravel new perspectives on understanding the physics underlying concrete spalling. The thermo-hydro-chemical code developed in this paper is made available in a GitHub repository.

Keywords TH model · Young's age concrete · Stoichiometric-based model · High temperature · Concrete drying · Experimental and numerical validation

1 Introduction

Understanding and predicting mid- and long-term concrete behavior is particularly important in civil engineering applications such as nuclear containment structures or tunnels [1–6]. Indeed, such structures can be subjected to an increase of temperature both in service conditions (e.g. radioactive waste storage [7]) or in accidental situations (e.g. fire in a tunnel [8]). The processes occurring in concrete at high-temperatures are the result of complex coupled thermal, hygral, chemical, and mechanical interactions: free capillary and chemically bound water is released at elevated temperatures and increases the pore pressure [9–12]. The temperature gradient produces thermal stresses, which, presumably together with the pore pressure, result in mechanical damage and may lead to spalling, i.e. the detachment (violent or not) of layers of the surface of concrete exposed to high temperatures. This process reduces the working cross-section of the structural element and can expose the reinforcements, leading to structural failure. Due to the complexity of the phenomenon, as well as the limited experimental observations at the local scale, the current explanations of the fire spalling mechanism are largely qualitative and no general consensus on a single theory has been reached [10, 12].

The ongoing research effort in this context includes parametric full-scale tests of structural elements [13] as well as a few small-scale tests [14, 15]. These latter predominantly focus on point-wise measurements of Temperature, gas Pressure and Mass loss (PTM tests) through the use of transducers [16–18]. Besides the

intrinsic issues with the sparseness of datasets based on point-wise measurement, some doubts are cast on the influence that these invasive probes may have on the processes themselves, given that the reported observations can range by more than an order of magnitude (e.g. pressure is in the range 0.3–3.5 MPa) [19, 20]. More recently, full-field experimental tests by means of neutron and x-ray tomography have allowed new insights into moisture transport in heated concrete, quantifying the so-called moisture clog phenomenon and pointing out the influence of local heterogeneities such as aggregates on moisture transport [21–23]. Despite the many uncertainties, research has identified some main influencing parameters on the behavior of concrete at high temperatures such as concrete mix design, moisture content, heating rate, external loading, and nature, and geometry of aggregates [24].

On the theoretical/numerical side, multiphase-coupled models for partially saturated porous media have been developed [11, 25–27]. These approaches are mainly based on thermodynamically constrained averaging theories, i.e. the fluid in the pores is considered as a two-phase fluid consisting of free water (capillary and adsorbed) and gas (vapor and dry air). Fluid transport is typically modeled by two Darcy-type laws (for liquid and gas advective velocities) and by Fick's law (for the diffusion of vapor within the gaseous phase) [27]. Despite some limitations (e.g. use of many phenomenological laws), existing numerical models proved quite effective in reproducing experimental results [11, 26, 28–30]. However, little to no attention is given to the initial material conditions, thus limiting the predictive capacities of these modeling strategies. Indeed, numerical models generally consider uniform initial conditions applied to a virgin-state material. Nevertheless, it is well-known that since casting and during its entire life, concrete is subjected to environmental and loading conditions such as temperature/humidity fluctuations or external loads that can affect its microstructure in terms of differential curing and moisture distribution, micro-cracks coalescence or creep [31].

In this regard, the role of the young age of concrete is critical, and it has been the subject of several numerical studies recently. You et al. [32, 33] have proposed a two stage hygro-thermo-mechanical model to study the shrinkage of concrete at early age. The model shared some of the hypothesis from

the approach described in the current work, however, there was no description of the dehydration process and the focus of the study was limited to low temperatures slightly above ambient conditions. Following the recent trend of proposing the use of machine learning algorithms allied with physical models, Liang et al. have studied the early age stress development in restrained concrete using active-ensemble learning within a thermo-chemo-mechanical framework [34]. The physical model adopted considered the Fourier law of heat transfer, an Arrhenius representation of the hydration reaction and a rate-type creep law for describing the mechanical behavior of concrete. The model was capable of reproducing the stresses measured experimentally and presented a promising approach for the complex problem of simulating the young age of concrete. However, as the maximum temperature considered in the models was limited to 40° C, no assessment of the dehydration behavior was provided. Finally, Prskalo et al. have proposed an extension of the Gawin's model of concrete to consider the effect of hygral phenomena in its early age behavior [35]. Once more, no extension to high temperatures is considered, confirming the current state-of-the-art in the numerical simulation of concrete: studies either disregard the transient nature of concrete and its historical evolution between casting and high temperature exposure, or are mainly focused on the room temperature conditions.

Indeed, the former category confirms that the hydration process itself may generate an inhomogeneous moisture content and/or material properties' distribution (e.g. porosity), depending on the geometry of the structure (e.g. a thick wall), the external environment (e.g. on two sides of a wall) or on the instant the accidental condition (e.g. fire) is applied.

The objective of this work is to propose an enhanced, unified numerical framework to focus on the impact of the thermo-hydric (TH) initial state (both in terms of material properties and moisture content) on the mid and long-term material behavior in the particular case of an increase of temperature. This is not possible with the state-of-the-art thermohygro models for concrete at high temperature, in which the chemical state of the concrete throughout its whole history is usually defined solely as a function of the temperature, and the relative humidity is disregarded. Based on a stoichiometric-based approach (i.e. following Powers' studies [36]),

hydration processes are taken into account stemming from the material's formulation. This way the constitutive equations that represent the concrete hydration degree, its porosity, the moisture content and the other material parameters are directly derived from the composition of the concrete. The parameters of such equations can be calibrated experimentally by a set of simple experiments such as the calorimeter test to obtain the coefficients related to the hydration [37], and the mass transfer parameters can be easily obtained from thermogravimetry tests. This method is a promising alternative in contrast to the usual method of solely manually adjusting the constitutive laws to fit the data from PTM tests.

As a further objective of the study, the effect of temperature on sorption/desorption isotherms is taken into account consistently with the new modeling framework, properly accounting for chemical damage irreversibility of the porous microstructure. The enhanced method also provides an evolution law that overcomes inconsistencies and numerical deficiencies of the existing formulations, i.e. smoothing the well-known strong discontinuities around the critical temperature of water.

The paper is structured in three parts. In Sect. 2, the mathematical model used for simulating the aging and high temperature behaviors of concrete is presented. Besides the concrete formulation, the model requires some characterization experiments to properly calibrate the stoichiometric approach, such as the calorimeter results for obtaining the hydration kinetics parameters and thermogravimetry for calibrating the constitutive laws related to the mass transfer. In the current work, the hydration parameters found in [37] were considered. Then, in Sect. 3 three cases are presented: first the current implementation is validated considering the hydration of cement in a high performance concrete at room temperatures, as described by Sciumè et al. [37]. Next, the model's predictive capacity for estimating the evolution of temperature and gas pressure is benchmarked with the results by Kalifa et al. [16]. The effect of different curing ages on this test is also considered. The third example considers a mass loss test experiment [38] reinforcing how the model proposed herein is capable of describing the behavior of different concrete compositions during temperature increase, as well as assessing the effect of different aging histories of the

concrete. Finally, Sect. 4 presents the main conclusions and impacts of the current work.

2 Mathematical model

2.1 Balance conservation equations

The model is based on the hybrid mixture theory for porous media in the mathematical formulation originally proposed in Hassanizadeh and Gray [39–41] and then applied for geomaterials [42] and concrete [43]. In this approach, the microstructure of the concrete is analyzed as a fully homogenized continuum, avoiding the explicit treatment of complex features of concrete such as the interfacial transition zone (ITZ). In fact, it was demonstrated experimentally by Dalton et al. that the mass transport dynamics of water within concrete does not show any influence of the ITZ, rendering its neglect a reasonable assumption [44]. The porous medium is regarded as an (eventually) deformable solid matrix (*s*) filled with the fluid phases, i.e. liquid water (*l*), vapor water (*v*) and dry air (*a*). Some typical hypotheses are introduced in the model: the velocity of the solid phase is negligible compared to those of the fluid phases, gases as well as their mixtures are considered as ideal, and the gravity effect is negligible. For the sake of brevity, only the final form of the macroscopic conservation equations is given, i.e.:

Solid phase:

$$\frac{\partial m_s}{\partial t} = \dot{m}_{hyd} \quad (1)$$

Liquid water phase:

$$\frac{\partial m_l}{\partial t} + \nabla \cdot (m_l v_{l-s}) = -\dot{m}_{vap} - \dot{m}_{hyd} \quad (2)$$

Vapor water phase:

$$\frac{\partial m_v}{\partial t} + \nabla \cdot (m_v v_{g-s}) + \nabla \cdot (m_v v_{v-g}) = \dot{m}_{vap} \quad (3)$$

Dry air phase:

$$\frac{\partial m_a}{\partial t} + \nabla \cdot (m_a v_{g-s}) + \nabla \cdot (m_a v_{a-g}) = 0 \quad (4)$$

where m_α is the mass per unit volume of phase α :

$$\begin{aligned} m_s &= (1 - \phi)\rho_s & m_l &= \rho_l S_l \phi \\ m_v &= \rho_v (1 - S_l)\phi & m_a &= \rho_a (1 - S_l)\phi \end{aligned} \quad (5)$$

The source term \dot{m}_{vap} corresponds to the water mass per unit-volume of porous medium and per unit-time due to evaporation ($\dot{m}_{vap} > 0$) or condensation ($\dot{m}_{vap} < 0$). The source term \dot{m}_{hyd} the water mass per unit-volume of porous medium and per unit-time due to hydration ($\dot{m}_{hyd} > 0$) or dehydration ($\dot{m}_{hyd} < 0$). The mass flux terms can be written as follows, i.e. by introducing Darcy's and Fick's transport laws:

$$m_v v_{g-s} + m_v v_{v-g} = -K \frac{\rho_v k_{rg}}{\mu_g} \nabla p_g - D \rho_g \frac{M_v M_a}{M_g^2} \nabla \ln \left(\frac{p_v}{p_g} \right) \quad (6)$$

$$m_a v_{g-s} + m_a v_{a-g} = -K \frac{\rho_a k_{rg}}{\mu_g} \nabla p_g - D \rho_g \frac{M_v M_a}{M_g^2} \nabla \left(\frac{p_a}{p_g} \right) \quad (7)$$

With respect to the thermal energy conservation equation, the averaging procedure gives:

$$\begin{aligned} \overline{\rho C_p} \frac{\partial T}{\partial t} + (m_l C_{p,l} v_{l-s} + m_g C_{p,g} v_{g-s}) \cdot \nabla T \\ + \nabla \cdot q = -H_{vap} \dot{m}_{vap} + H_{hyd} \dot{m}_{hyd} \end{aligned} \quad (8)$$

where the heat capacity of the whole porous medium is:

$$\sum_{i=a,v,l,s} (m_i C_{p,i}) = \overline{\rho C_p} \quad (9)$$

It is worth noting that the second and third term in this relationship provides the advective and diffusive heat transfers in the medium, while the heat flux term is typically given by Fourier's law:

$$- \lambda \cdot \nabla T \quad (10)$$

Balance equations are supplemented by an appropriate set of constitutive laws for model closure and describing the physical processes. Since the objective of the paper is to estimate the early age and aging behavior over an accidental condition such as a temperature rise, not all the constitutive laws are given. The interested reader can make reference to previous papers by the same authors (see e.g. [45–47]).

2.2 Cement paste hydration and aging: extension to high temperatures

The chemical model describing cement hydration and aging is based on the works by Sciumè et al. [45]. The cement hydration degree ξ is introduced as the mass ratio between the hydrated cement $c_{hyd}(t)$ at time t and the initial, total cement c :

$$\xi(t) = \frac{c_{hyd}(t)}{c} \quad (11)$$

High performance concrete is characterized by a low w/c ratio, which implies that only a fraction of the cement in the mix will be hydrated, thus giving $\xi_\infty < 1$ at $t \rightarrow \infty$. For this reason, the hydration degree of the sample Γ , i.e. the ratio between the chemically bound water at time t , $m_{hyd}(t)$, and the chemically bound water at $t \rightarrow \infty$, i.e. m_{hyd}^∞ , is introduced and will be adopted in the later developments:

$$\Gamma(t) = \frac{m_{hyd}(t)}{m_{hyd}^\infty} \quad (12)$$

The cement hydration degree, $\xi(t)$, and the hydration degree of the sample, $\Gamma(t)$, are indeed related as follows:

$$\xi(t) = \xi_\infty \Gamma(t) \quad (13)$$

The hydration degree $\Gamma(t)$ allows describing the full hydration (and dehydration) process of the cement paste and constitutes the main internal variable of the thermohydrochemical (THC) model. Indeed, the microstructure evolution is closely related to the products of the hydration reaction and consequently, to the degree of hydration, Γ [45].

The cement hydration reaction is a thermo-activated process that is commonly described by means of an Arrhenius-type evolution relationship:

$$\frac{d\Gamma}{dt} = A_\Gamma \beta_{RH} \exp\left(-\frac{E_a}{RT}\right) \quad (14)$$

where $A_{(\Gamma)}$ is the macroscopic chemical affinity (given in [45]), E_a is the hydration activation energy, β is a function of the relative humidity RH , taking into account its effect on the hydration process. Notice that the chemical affinity is itself a function of the hydration degree. Thus, in the current numerical implementation, a fourth equation of evolution of Γ

will be considered, where G is an internal variable that represents the hydration degree, as described by Gawin et al. [27].

The hydration degree is impacted when concrete is exposed to high temperatures (typically $T > 100^\circ\text{C}$): hydrates transform into less hydrated components, free water is released into the porous network and the material microstructure is strongly altered in terms of transport (porosity, sorption/desorption isotherms), heat transfer (dehydration is an endothermic phenomenon) and phases' properties. According to the previous definitions, dehydration and hydration are consistently defined by introducing a dehydration degree F , that, combined with Γ defines the effective hydration degree $\tilde{\Gamma}$:

$$\tilde{\Gamma} = (1 - F)\Gamma \quad (15)$$

The coupled evolution model is therefore expressed by the following relationship:

$$\frac{d\tilde{\Gamma}}{dt} = (1 - F)\frac{d\Gamma}{dt} - \Gamma\frac{dF}{dt} \quad (16)$$

Since the rate of dehydration is irreversible, the following condition should be fulfilled:

$$\frac{dF}{dt} = \begin{cases} \frac{\partial F(T)}{\partial T} \left\langle \frac{dT}{dt} \right\rangle_+ & \text{with } T(t) > T_{max}(t) \\ 0 & \text{with } T(t) < T_{max}(t) \end{cases} \quad (17)$$

The parameter $F(T)$ can then be introduced according to different relationships, such as the following one proposed by Pesavento et al. [26]:

$$F(T) = \begin{cases} 0, & \text{with } T < 105^\circ\text{C} \\ \frac{[1 + \sin(\pi/2 (1 - 2 \exp(a_1^f (T - 105))))]}{2}, & \text{with } T > 105^\circ\text{C} \end{cases} \quad (18)$$

where $a_1^f = -0.004$ was found to reproduce the behavior of the concrete tested in Kalifa et al. [16], whereas $a_1^f = -0.008$ was the value calibrated for the composition studied by Kanema et al. [38]. The definition of the dehydration degree should be described according to experimental evidence. Other empirical relationships are also available in the literature (see e.g. [21, 27, 48]).

Once the effective degree of hydration $\tilde{\Gamma}$ is defined, Powers' volumetric model is here retained to quantify the phase composition of a hardening

Portland cement paste, eventually with silica-fume addition [36]. The full set of equations is described as follows (Table 1):

where $\sum_i V_i = 1$ and the initial volume fraction of water in the mixture is given by:

$$p = \frac{w/c}{w/c + \rho_w/\rho_c + (\rho_w/\rho_{sf})(s/c)} \quad (19)$$

Finally, the parameter k is defined as:

$$k = \frac{1}{1 + \rho_c/\rho_{sf}(s/c)} \quad (20)$$

Cement's hydration is characterized by Le Chatelier's contraction, i.e. chemical shrinkage given by the first equation of Powers' model as well as the formation of a gas volume related to cement paste self-dessication. The theoretical upper limit value for the hydrated cement fraction ξ_∞ is calculated by imposing zero capillary water, i. e. $V_{cw} = 0$, thus having:

$$\xi_\infty = \min \left\{ \frac{p}{k[1.32 + 1.57(s/c)](1-p)}, 1 \right\} \quad (21)$$

The value of ξ_∞ is indeed greater than the real hydration fraction ξ_∞ , that is estimated by empirical equations such as the one proposed by Mills et al. [49]:

$$\xi_\infty^{Mills} = \frac{1.031(w/c)}{0.194 + (w/c)} \quad (22)$$

Powers' model gives the total amount of chemically bound water directly derived from concrete formulation/stoichiometry. After some manipulations and assuming $\xi_\infty = \xi_\infty^{Mills}$, the maximum bound water content can be defined as follows:

$$m_{hyd}^\infty = 0.228c\xi_\infty \quad (23)$$

Table 1 Powers' model description of volume fraction of each phase in concrete

Chemical shrinkage	$V_{cs} = k(0.20 + 0.69(s/c))(1-p)\xi$
Capillary water	$V_{cw} = p - k(1.32 + 1.57(s/c))(1-p)\xi$
Gel water	$V_{gw} = k(0.60 + 1.57(s/c))(1-p)\xi$
Gel solid	$V_{gs} = k(1.52 + 0.74(s/c))(1-p)\xi$
Cement	$V_c = k(1-p)\xi$
Silica fume	$V_s = k(1.43(s/c))(1-p)(1-\xi)$

The rate of hydration water consumption is then:

$$\dot{m}_{hyd} = 0.228c\xi_\infty \frac{d\tilde{\Gamma}}{dt} \quad (24)$$

The heat release associated with hydration/dehydration is taken into account by the term $H_{hyd} \dot{m}_{hyd}$ that can expressed as:

$$H_{hyd} \dot{m}_{hyd} = L_{hyd} \frac{d\tilde{\Gamma}}{dt} \quad (25)$$

where $L_{hyd} = 0.228c\xi_\infty H_{hyd}$ is the latent heat of hydration that is usually estimated from adiabatic calorimetry.

2.3 Porosity evolution

The total porosity of the cement paste can be directly obtained by Powers' model by assuming ξ_∞ as a function of the effective hydration degree $\tilde{\Gamma}(t)$, i.e. by summing the chemical shrinkage, the capillary and gel water volume fractions:

$$\phi(\tilde{\Gamma}) = \phi_\infty^{cp} \Omega + a_\phi(1 - \tilde{\Gamma}) \Omega + \phi^{As} (1 - \Omega) \quad (26)$$

where Ω is the volume of the cement paste, ϕ^{As} is the average porosity of the aggregates (usually neglected) and ϕ_∞^{cp} is the final value of the cement paste porosity after curing. ϕ_∞^{cp} and a_ϕ are given by:

$$\phi_\infty^{cp} = p - k[0.52 - 0.69(s/c)](1-p) \xi_\infty \quad (27)$$

$$a_\phi = k[0.52 - 0.69(s/c)](1-p) \xi_\infty \quad (28)$$

2.4 Sorption/desorption isotherms

Sorption/desorption isotherms play a crucial role in porous media modelling and concrete at high temperature in particular [12, 30, 50]. The relationship proposed by Baroghel-Bouny [51] is commonly adopted when describing the saturation-capillary pressure relationship at ambient temperature:

$$p_c = p_c(S_i) = a(S_i^{-b} - 1)^{\left(1 - \frac{1}{i}\right)} \quad (29)$$

the coefficients a and b are fitting parameters related to the material type. Pesavento [26] proposed an extension of the above formulation to take into account high temperatures. That was extensively

used by multiple authors such as Gawin et al. [27]. However, the functions developed for the coefficient a in this formulation is only continuous by parts and as the numerical formulation of the model relies on derivatives of the saturation degree, this poses numerical challenges, specially around the critical temperature of water. This can be observed in Fig. 1.

More recently, Drouet et al. experimentally quantified the evolution of the desorption isotherms in the range between 20°C and 80°C [52]. Davie et al. implemented these measurements in a formulation considering the effect of temperature by accounting for porosity, surface tension and permeability evolution while heating [53]. However, this latter formulation turns out to be inconsistent for high temperatures (above 100°C). Dauti et al. [54] proposed an inverse analysis based on neutron tomography observations to identify retention curves above 100°C .

Though experimental evidence is still missing in the high temperature range, retention curves are indeed related to water surface tension γ^w and microstructure evolution, i.e. in the proposed model the microstructure evolution is described by the effective hydration degree $\tilde{\Gamma}$.

The following formulation is therefore proposed:

$$a(T, \tilde{\Gamma}) = a_0 \left(\frac{\tilde{\Gamma} + a_1^a}{1 + a_1^a} \right)^{a_2^a} \frac{\gamma^w(T) + a_3^a \gamma_0^w}{(1 + a_3^a) \gamma_0^w} \quad (30)$$

where $a_1^a = 0.1$, $a_2^a = 1.5$, $a_3^a = 0.05$ for the composition in Kanema's test and for the Kalifa's one, $a_1^a = 0.1$ and $a_2^a = 1.5$ and the last term was disregarded.

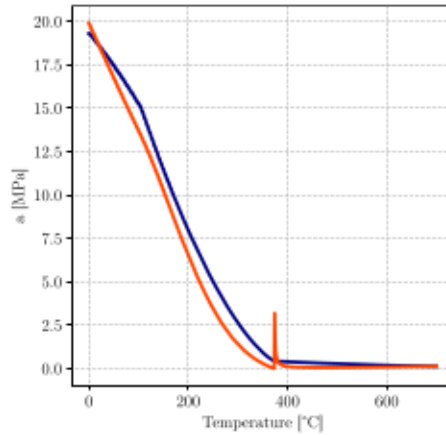
Giving the following $S_l - p_c$ relationship:

$$S_l(p_c, T, \tilde{\Gamma}) = \left[\left(\frac{p_c}{a(T, \tilde{\Gamma})} \right)^{\frac{b}{b-1}} + 1 \right]^{-\frac{1}{b}} \quad (31)$$

The use of $a(T, \tilde{\Gamma})$ yields a function that does not show the noticeable jump around the critical temperature of water, as showed in Fig. 1.

2.5 Model calibration overview

The complete set of required constitutive equations can be found in Appendix A. These equations involve material parameters which usually are calibrated with *ad hoc* experiments [11, 27, 30, 55].



$$\begin{aligned}
 & \text{--- } a(T, \tilde{\Gamma}) = a_0 \left(\frac{\tilde{\Gamma} + 0.1}{1.1} \right) \frac{\gamma^w(T) + 0.05 \gamma_0^w}{1.05 \gamma_0^w} \\
 & \text{--- } a(T) = \begin{cases} \left(\frac{T_{crit} - T_0}{T_{crit} - T} \right)^N \frac{1}{a_0} & \text{if } T \leq 100^\circ\text{C} \\ \left(\frac{T_{crit} - T_0}{T_{crit} - T} \right)^N \left((Q_3 - Q_2) \left[2 \left(\frac{T - T_b}{T_{crit} - T_b} \right)^3 - 3 \left(\frac{T - T_b}{T_{crit} - T_b} \right)^2 + 1 \right] + Q_2 \right)^{-1} & \text{if } 100^\circ\text{C} < T < 373.15^\circ\text{C} \\ \left[\frac{N}{2} E_0 T + \left(E_0 - \frac{N}{2} E_0 (T_{crit} - z) \right) \right] \left((Q_3 - Q_2) \left[2 \left(\frac{T - T_b}{T_{crit} - T_b} \right)^3 - 3 \left(\frac{T - T_b}{T_{crit} - T_b} \right)^2 + 1 \right] + Q_2 \right)^{-1} & \text{if } T \geq 373.15^\circ\text{C} \end{cases}
 \end{aligned}$$

Fig. 1 Comparison of the currently proposed saturation degree coefficient law and the one adopted by Gawin et al. [27]

Fig. 2 Overview of the experiments required for obtaining and/or calibrating the properties considered in the proposed model

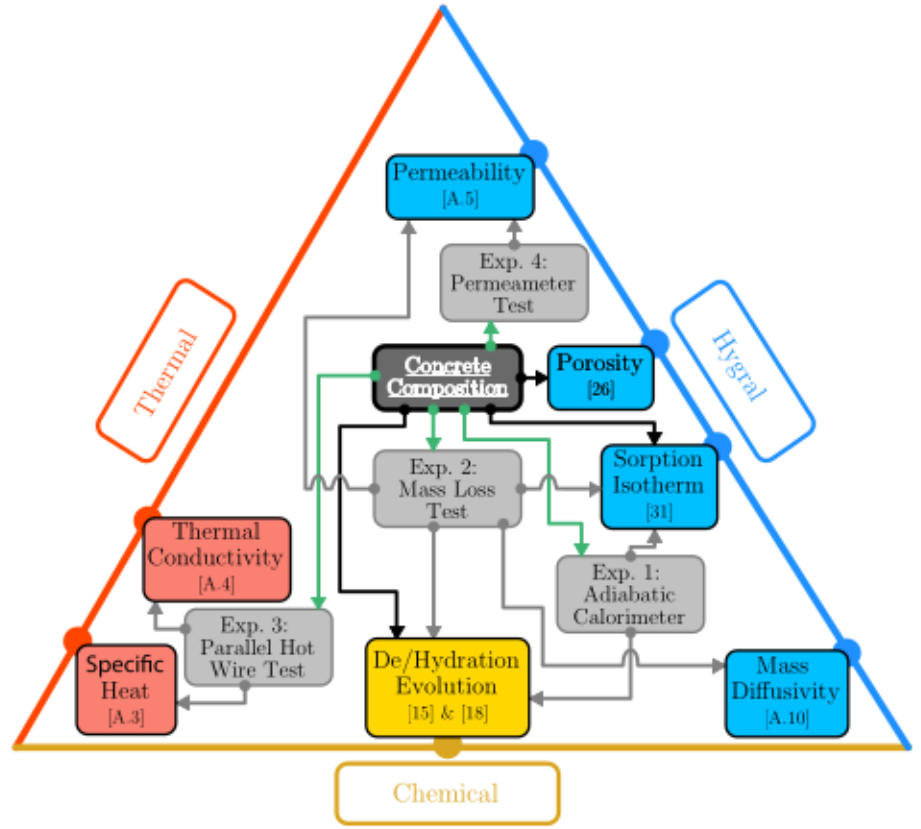


Figure 2 summarizes the process for the identification of the input parameters for the proposed model. Starting from the concrete composition (dark grey box), the parameters related to the evolution of porosity during hydration (*cf.* eq.(26)) as well as the amount of water required for cement hydration, can be obtained via the adopted stoichiometry-based approach. Consequently, only four experiments (grey boxes) are needed to identify the parameters associated with thermal (red boxes), hygral (blue boxes) and chemical (yellow boxes) constitutive relationships respectively.

More specifically, the set of experiments includes:

- *Adiabatic (or semi-adiabatic) calorimetry test (Exp. 1)*. Such test is required to identify the parameters of the average chemical affinity function from self-heating of the analyzed sample [37]. The degree of reaction can be indeed expressed as the ratio between the total heat released at a given moment $Q_{hydr}(t)$ and the heat released for the full concrete hydration $Q_{hydr}(t \rightarrow \infty)$:

$$\Gamma(t) = \frac{Q_{hydr}(t)}{Q_{hydr}(t \rightarrow \infty)} \quad (32)$$

- *Permeability test (Exp. 2)*. This test is performed with a standard equipment such as the Cembureau apparatus.
- *Mass loss test (Exp. 3)*. Such test is needed to identify transport properties as vapor effective diffusivity and calibrate the relative permeability functions as well as the sorption isotherm model.
- *Thermal characterization (Exp. 4)*. The thermal properties can be directly measured by means of some common devices, e.g. the parallel hot wire test is often adopted due to its representativeness of the heterogeneous microstructure of concrete. It should be noted that in the herein proposed case, Kanema et al. have adopted the thermal constitutive laws from Eurocodes [38].

The depicted procedure is quite robust to characterize the evolution of material parameters during concrete hydration ([37]). However, the fine assessment

of how the permeability and sorption properties evolve upon high temperature could fall short for relatively high temperatures, i.e. when the impact of microcracking on transport and sorption properties becomes important. A possible workaround to enhance the calibration process is constituted by the use of full-field techniques such as neutron tomography [22, 30] at high temperature. Such tests have been already adopted in previous works and could further aid the calibration of permeability, porosity and sorption isotherms.

2.6 Final form of the conservation equations

The mathematical problem is now defined considering the three conservation equations (mass balance of dry air, of water and enthalpy balance) and also the evolution equation of the dehydration degree, yielding a system of equations with 3 state variables, the gas pressure, p_g , the capillary pressure, p_c , and temperature, T , and one internal variable, the hydration degree G . Thus, the following developments will consider the conservation equations as functions of the primary variables in order to obtain its final form which will be ultimately solved by the finite element method.

Equation (1) allows obtaining the following relationship for porosity evolution:

$$\frac{\partial \phi}{\partial t} = \frac{1}{\rho_s} \left[(1 - \phi) \frac{\partial \rho_s}{\partial \tilde{\Gamma}} \frac{\partial \tilde{\Gamma}}{\partial t} - \dot{m}_{hyd} \right] \quad (33)$$

Powers model allows writing (see eq. 26):

$$\frac{\partial \phi}{\partial t} = \frac{1}{\rho_s} \left[(1 - \phi) \frac{\partial \rho_s}{\partial \tilde{\Gamma}} - 0.228c\xi_\infty \right] \frac{\partial \tilde{\Gamma}}{\partial t} \quad (34)$$

Furthermore, it can be proved that the relationship can be further simplified as follows:

$$\frac{\partial \phi}{\partial t} = -a_\phi \Omega \frac{\partial \tilde{\Gamma}}{\partial t} \quad (35)$$

where a_ϕ is a constant parameter that governs the evolution of porosity due to hydration/dehydration.

We can therefore write, for each phase, the following equations by applying the derivatives chain rule and injecting relationship 35:

• Liquid phase:

$$S_l \rho_l \left(-a_\phi \Omega \frac{\partial \tilde{\Gamma}}{\partial t} \right) + S_l \phi \frac{\partial \rho_l}{\partial t} + \rho_l \phi \frac{\partial S_l}{\partial t} + \nabla \cdot (m_l v_{l-s}) = -\dot{m}_{vap} - \dot{m}_{hyd} \quad (36)$$

• Vapor phase:

$$(1 - S_l) \rho_v \left(-a_\phi \Omega \frac{\partial \tilde{\Gamma}}{\partial t} \right) + (1 - S_l) \phi \frac{\partial \rho_v}{\partial t} - \rho_v \phi \frac{\partial S_l}{\partial t} + \nabla \cdot (m_v v_{g-s}) + \nabla \cdot (m_v v_{v-g}) = \dot{m}_{vap} \quad (37)$$

• Dry air:

$$(1 - S_l) \phi \frac{\partial \rho_a}{\partial t} - \rho_a \phi \frac{\partial S_l}{\partial t} + \nabla \cdot (m_a v_{g-s}) + \nabla \cdot (m_a v_{a-g}) - (1 - S_l) \rho_a \left(a_\phi \Omega \frac{\partial \tilde{\Gamma}}{\partial t} \right) = 0 \quad (38)$$

Fluid phases equations can then be summed giving the water phase conservation equation:

• Total water phase:

$$(1 - S_l) \phi \frac{\partial \rho_v}{\partial t} + S_l \phi \frac{\partial \rho_l}{\partial t} + (\rho_l - \rho_v) \phi \frac{\partial S_l}{\partial t} + \nabla \cdot (m_l v_{l-s}) + \nabla \cdot (m_v v_{g-s}) + \nabla \cdot (m_v v_{v-g}) = [S_l \rho_l + (1 - S_l) \rho_v] \left(a_\phi \Omega \frac{\partial \tilde{\Gamma}}{\partial t} \right) - 0.228c\xi_\infty \frac{\partial \tilde{\Gamma}}{\partial t} \quad (39)$$

The previous equations are now developed with respect to the state and internal variables. Darcy's, Fick's and Fourier's laws are injected in the relationships thus giving the final form of the state equations:

• Dry air:

$$\begin{aligned} & \phi(1 - S_l) \left(\frac{\partial \rho_a}{\partial T} \frac{\partial T}{\partial t} + \frac{\partial \rho_a}{\partial p_c} \frac{\partial p_c}{\partial t} + \frac{\partial \rho_a}{\partial p_g} \frac{\partial p_g}{\partial t} \right) \\ & - \phi \rho_a \left(\frac{\partial S_l}{\partial T} \frac{\partial T}{\partial t} + \frac{\partial S_l}{\partial p_c} \frac{\partial p_c}{\partial t} + \frac{\partial S_l}{\partial \tilde{\Gamma}} \frac{\partial \tilde{\Gamma}}{\partial t} \right) \\ & - \nabla \cdot \left(K \frac{\rho_a k_{rg}}{\mu_g} \nabla p_g \right) - \nabla \cdot \left(D \rho_g \frac{M_v M_a}{M_g^2} \nabla \left(\frac{p_a}{p_g} \right) \right) \\ & = (1 - S_l) \rho_a \left(a_\phi \Omega \frac{\partial \tilde{\Gamma}}{\partial t} \right) \end{aligned} \quad (40)$$

• Total water:

$$\begin{aligned}
& \phi(\rho_l - \rho_v) \left(\frac{\partial S_l}{\partial T} \frac{\partial T}{\partial t} + \frac{\partial S_l}{\partial p_c} \frac{\partial p_c}{\partial t} + \frac{\partial S_l}{\partial \tilde{\Gamma}} \frac{\partial \tilde{\Gamma}}{\partial t} \right) \\
& + (1 - S_l) \phi \left(\frac{\partial \rho_v}{\partial T} \frac{\partial T}{\partial t} + \frac{\partial \rho_v}{\partial p_c} \frac{\partial p_c}{\partial t} + \frac{\partial \rho_v}{\partial p_g} \frac{\partial p_g}{\partial t} \right) \\
& + S_l \phi \frac{\partial \rho_l}{\partial T} \frac{\partial T}{\partial t} - \nabla \cdot \left(K \frac{\rho_l k_{rl}}{\mu_l} (\nabla p_g - \nabla p_c) \right) \\
& - \nabla \cdot \left(K \frac{\rho_v k_{rg}}{\mu_g} \nabla p_g \right) - \nabla \cdot \left(D \rho_g \frac{M_v M_a}{M_g^2} \nabla \left(\frac{p_v}{p_g} \right) \right) \\
& = [S_l \rho_l + (1 - S_l) \rho_v] \left(a_\phi \Omega \frac{\partial \tilde{\Gamma}}{\partial t} \right) - 0.228 c_\infty^\epsilon \frac{\partial \tilde{\Gamma}}{\partial t}
\end{aligned} \tag{41}$$

• Energy conservation:

$$\begin{aligned}
& \overline{\rho C_p} \frac{\partial T}{\partial t} + K \left(C_{\rho_l} \frac{\rho_l k_{rl}}{\mu_l} (\nabla p_g - \nabla p_c) + C_{\rho_g} \frac{\rho_v k_{rg}}{\mu_g} \nabla p_g \right) \cdot \nabla T \\
& - \nabla \cdot (\lambda \cdot \nabla T) - H_{vap} S_l \phi \frac{\partial \rho_l}{\partial T} \frac{\partial T}{\partial t} \\
& - H_{vap} \rho_l \phi \left(\frac{\partial S_l}{\partial T} \frac{\partial T}{\partial t} + \frac{\partial S_l}{\partial p_c} \frac{\partial p_c}{\partial t} + \frac{\partial S_l}{\partial \tilde{\Gamma}} \frac{\partial \tilde{\Gamma}}{\partial t} \right) \\
& - H_{vap} \nabla \cdot \left(K \frac{\rho_l k_{rl}}{\mu_l} (\nabla p_g - \nabla p_c) \right) \\
& = -H_{vap} S_l \rho_l \left(a_\phi \Omega \frac{\partial \tilde{\Gamma}}{\partial t} \right) \\
& + (H_{vap} 0.228 c_\infty^\epsilon + L_{hyd}) \frac{d\tilde{\Gamma}}{dt}
\end{aligned} \tag{42}$$

Finally, the evolution equation is also considered, where G is an internal variable used to compute the value of $\Gamma(t)$ explicitly, yielding the mathematical problem based on the system of Equations (40 - 43).

• Evolution of the hydration degree:

$$\frac{\partial \Gamma}{\partial t} = \frac{\partial G}{\partial t} \tag{43}$$

2.7 Boundary conditions

The hygro-thermal problem is solved by satisfying the conservation eq. (40), (42) and (41) in the domain Ω with the following boundary conditions on Σ [56]:

$$p_g = \bar{p}_g \text{ on } \Sigma_p \tag{44}$$

$$p_c = \bar{p}_c \text{ on } \Sigma_p \tag{45}$$

$$T = \bar{T} \text{ on } \Sigma_T \tag{46}$$

$$-J_{v-s} \cdot n = \bar{q}_v - h_g (\rho_v - \rho_v^\infty) \text{ on } \bar{\Sigma}_p \tag{47}$$

$$-J_{a-s} \cdot n = \bar{q}_a - h_g (\rho_a - \rho_a^\infty) \text{ on } \bar{\Sigma}_p \tag{48}$$

$$-J_{l-s} \cdot n = \bar{q}_l \text{ on } \bar{\Sigma}_p \tag{49}$$

$$-(q - H_{vap} J_{l-s}) \cdot n = \bar{q}_T - h_T (T - T_\infty) - f \sigma (T^4 - T_\infty^4) \text{ on } \bar{\Sigma}_T \tag{50}$$

where Σ_p is part of the boundary at which the pressures and the temperature are known (Dirichlet type boundary conditions) while $\bar{\Sigma}_p$ is the complementary part (with unit outward normal n) at which the mass fluxes of fluids and heat flux are imposed.

The prescribed fluxes of vapor and air are represented by \bar{q}_π with $\pi = v, a$, ρ_π^∞ is the densities of vapor and dry air, the temperature in the far field surrounding gas is given by T_∞ , while h_g and h_T are the convective mass/energy exchange coefficient, respectively [56]. ϵ is the emissivity and σ is the Stefan–Boltzmann constant.

Moreover, the initial conditions $p_g(x, t = 0)$, $p_c(x, t = 0)$, $T(x, t = 0)$, and $G(x, t = 0)$ are also to be specified, where x is the vector of spatial coordinates.

The right-hand-side of eq. (50) gives the interface exchange between a porous medium and the surrounding fluid (i.e. moist air) and the second left-hand-side term gives the energy exchange due to vaporization.

It is worth noting that the introduction of mass convective boundary conditions (47) and (48) requires developing the mass densities in terms of the problem state variables (p_c , p_g , T). Nevertheless, the relationships relating the densities to the state variables are strongly non-linear which does not permit to obtain a straightforward algebraic form of these boundary conditions, suitable for the discretized problem. For a given time station t , the relationships relating the densities to the state variables are linearized at the neighborhood of a reference time station t_{ref} :

$$\rho_x \approx \rho_x^{ref} + \frac{\partial \rho_x}{\partial p_g} (p_g - p_g^{ref}) + \frac{\partial \rho_x}{\partial p_c} (p_c - p_c^{ref}) + \frac{\partial \rho_x}{\partial T} (T - T^{ref}) \quad (51)$$

where $(p_c, p_g, T)_{ref}$ are the values of the variables at t_{ref} . The choice of the reference time will depend on the adopted iterative algorithm. Finally, homogenous Neumann boundary conditions are considered for the evolution of the reaction degree equation, as described by Eq. (52).

$$\nabla G \cdot n = 0 \quad \text{on } \Sigma_T \cup \bar{\Sigma}_T \cup \Sigma_p \cup \bar{\Sigma}_p \quad (52)$$

2.8 Finite element formulation and implementation

The weak form of Eqs (53 - 55) reads, after some manipulations:

$$\begin{aligned} & \int_{\Omega} p_g^* \left(-\phi \rho_a \frac{\partial S_l}{\partial T} + \phi (1 - S_l) \frac{\partial \rho_a}{\partial T} \right) \frac{\partial T}{\partial t} d\Omega \\ & + \int_{\Omega} p_g^* \phi (1 - S_l) \frac{\partial \rho_a}{\partial p_g} \frac{\partial p_g}{\partial t} d\Omega \\ & + \int_{\Omega} p_g^* \left(\phi (1 - S_l) \frac{\partial \rho_a}{\partial p_c} - \phi \rho_a \frac{\partial S_l}{\partial p_c} \right) \frac{\partial p_c}{\partial t} d\Omega \\ & + \int_{\Omega} \left(K \frac{\rho_a^{k_{rg}}}{\mu_g} - D \frac{M_v M_a}{M_g RT} \left(\frac{\rho_v}{\rho_l} - \frac{p_v}{p_g} \right) \right) \nabla p_g^* \nabla p_g d\Omega \\ & + \int_{\Omega} D \frac{M_v M_a}{M_g RT} \frac{\rho_v}{\rho_l} \nabla p_g^* \nabla p_c d\Omega \\ & - \int_{\Omega} D \frac{M_v M_a}{M_g RT} \frac{\partial p_v}{\partial T} \nabla p_g^* \nabla T d\Omega \\ & - \int_{\Omega} \nabla p_g^* \cdot \left[(1 - S_l) \rho_a a_\phi + \rho_a \phi \frac{\partial S_l}{\partial \bar{\Gamma}} \right] \frac{\partial \bar{\Gamma}}{\partial t} d\Omega \\ & = \int_{\bar{\Sigma}_p} p_g^* (\bar{q}_a - h_g (\rho_a - \rho_a^\infty)) d\Sigma \end{aligned} \quad (53)$$

$$\begin{aligned} & \int_{\Omega} p_c^* \left(S_l \phi \frac{\partial \rho_l}{\partial T} + (1 - S_l) \phi \frac{\partial \rho_v}{\partial T} + \phi (\rho_l - \rho_v) \frac{\partial S_l}{\partial T} \right) \frac{\partial T}{\partial t} d\Omega \\ & + \int_{\Omega} p_c^* \phi \left((1 - S_l) \frac{\partial \rho_v}{\partial p_c} + (\rho_l - \rho_v) \frac{\partial S_l}{\partial p_c} \right) \frac{\partial p_c}{\partial t} d\Omega \\ & + \int_{\Omega} p_c^* \phi (1 - S_l) \frac{\partial \rho_v}{\partial p_g} \frac{\partial p_g}{\partial t} d\Omega \\ & - \int_{\Omega} \left(K \frac{\rho_l^{k_{rl}}}{\mu_l} + D \frac{M_v M_a}{M_g RT} \frac{\rho_v}{\rho_l} \right) \nabla p_c^* \nabla p_c d\Omega \\ & + \int_{\Omega} \left(K \left(\frac{\rho_l^{k_{rl}}}{\mu_l} + \frac{\rho_v^{k_{rg}}}{\mu_g} \right) + D \frac{M_v M_a}{M_g RT} \left(\frac{\rho_v}{\rho_l} - \frac{p_v}{p_g} \right) \right) \\ & \nabla p_c^* \nabla p_g d\Omega + \int_{\Omega} D \frac{M_v M_a}{M_g RT} \frac{\partial p_v}{\partial T} \nabla p_c^* \nabla T d\Omega \\ & - \int_{\Omega} \left[[S_l \rho_l + (1 - S_l) \rho_v] a_\phi + 0.228 c \xi_\infty + \phi (\rho_l - \rho_v) \frac{\partial S_l}{\partial \bar{\Gamma}} \right] \frac{\partial \bar{\Gamma}}{\partial t} d\Omega \\ & = \int_{\tau} p_c^* \cdot (\bar{q}_l + \bar{q}_v - h_g (\rho_v - \rho_v^\infty)) d\Sigma \end{aligned} \quad (54)$$

$$\begin{aligned} & \int_{\Omega} T^* \left(\overline{\rho C_p} - H_{vap} \cdot \phi S_l \frac{\partial \rho_l}{\partial T} - H_{vap} \cdot \phi \rho_l \frac{\partial S_l}{\partial T} \right) \frac{\partial T}{\partial t} d\Omega \\ & + \int_{\Omega} T^* \left(H_{vap} \cdot \phi \rho_l \frac{\partial S_l}{\partial p_c} \right) \frac{\partial p_c}{\partial t} d\Omega \\ & + \int_{\Omega} T^* K \left(-C_{p,l} \frac{\rho_l^{k_{rl}}}{\mu_l} + C_{p,g} K \frac{\rho_g^{k_{rg}}}{\mu_g} \right) \cdot \nabla p_g \nabla T d\Omega \\ & + \int_{\Omega} T^* K C_{p,l} \frac{\rho_l^{k_{rl}}}{\mu_l} \cdot \nabla p_c \nabla T d\Omega \\ & - \int_{\Omega} H_{vap} \cdot K \frac{\rho_l^{k_{rl}}}{\mu_l} \nabla T^* \nabla p_g d\Omega \\ & + \int_{\Omega} H_{vap} \cdot K \frac{\rho_l^{k_{rl}}}{\mu_l} \nabla T^* \nabla p_c d\Omega + \int_{\Omega} \lambda \nabla T^* \nabla T d\Omega \\ & - \int_{\Omega} T^* H_{vap} \cdot \left(-S_l \rho_l a_\phi + \rho_l \phi \frac{\partial S_l}{\partial \bar{\Gamma}} + 0.228 c \xi_\infty \right) \frac{\partial \bar{\Gamma}}{\partial t} d\Omega \\ & = \int_{\tau} T^* (\bar{q}_T - h_T (T - T_\infty) - \int \sigma (T^4 - T_\infty^4)) d\Sigma \end{aligned} \quad (55)$$

$$\int_{\Omega} \left(\frac{\partial G}{\partial t} \right) G^* d\Omega = \int_{\Omega} \left(\frac{\partial \Gamma}{\partial t} \right) G^* d\Omega \quad (56)$$

where p_g^* , p_c^* , T^* and G^* , are test functions which are null on the boundary Σ_p and Σ_T respectively.

The unknown variables are expressed in terms of their nodal values as:

$$p_g(t) = \mathbf{N}_{p_g} \bar{\mathbf{p}}_g(t) \quad p_c = \mathbf{N}_{p_c} \bar{\mathbf{p}}_c(t) \quad T = \mathbf{N}_T \bar{\mathbf{T}}(t) \quad G = \mathbf{N}_G \bar{\mathbf{G}}(t)$$

where $\bar{\mathbf{p}}_g(t)$, $\bar{\mathbf{p}}_c(t)$, $\bar{\mathbf{T}}(t)$ and $\bar{\mathbf{G}}(t)$ are vectors of the nodal values of the primary variables at the time instant t , and \mathbf{N}_{p_g} , \mathbf{N}_{p_c} , \mathbf{N}_T and \mathbf{N}_G are the shape functions related to these variables. After the finite element discretization, the final system of equations can be expressed in the following matrix form:

$$\mathbf{C}_{ij}(\mathbf{Y}) \frac{\partial \mathbf{Y}}{\partial t} + \mathbf{K}_{ij}(\mathbf{Y}) \mathbf{Y} = \mathbf{f}_i(\mathbf{Y}) \quad (57)$$

with:

$$\mathbf{K}_{ij} = \begin{pmatrix} \mathbf{K}_{gg} & \mathbf{K}_{gc} & \mathbf{K}_{gt} & 0 \\ \mathbf{K}_{cg} & \mathbf{K}_{cc} & \mathbf{K}_{ct} & 0 \\ \mathbf{K}_{tg} & \mathbf{K}_{tc} & \mathbf{K}_{tt} & 0 \\ 0 & 0 & 0 & \mathbf{K}_{GG} \end{pmatrix}$$

$$\mathbf{C}_{ij} = \begin{pmatrix} \mathbf{C}_{gg} & \mathbf{C}_{gc} & \mathbf{C}_{gt} \\ 0 & \mathbf{C}_{cc} & \mathbf{C}_{ct} \\ 0 & \mathbf{C}_{tc} & \mathbf{C}_{tt} \\ 0 & 0 & 0 \end{pmatrix} \quad \mathbf{f}_i = \begin{pmatrix} \mathbf{f}_g \\ \mathbf{f}_c \\ \mathbf{f}_t \\ \mathbf{f}_G \end{pmatrix}$$

where $\mathbf{Y} = \{\bar{\mathbf{p}}_g, \bar{\mathbf{p}}_c, \bar{\mathbf{T}}, \bar{\mathbf{G}}\}$ is the approximated solution. It is worth noting that a linearization strategy is adopted to estimate the term $\mathbf{f}_\alpha^{n+\theta}$ for α :

$$\mathbf{f}_\alpha^{n+\theta} = \int_{\tilde{\Sigma}_p} \mathbf{N}^T \left(\bar{q}_\alpha^{n+\theta} - h_g^{n+\theta} (\rho_\alpha^{n+\theta} - \rho_\alpha^{\infty-n+\theta}) \right) \quad (58)$$

where $\alpha = v, a$ and $\rho_\alpha^{\infty-n+\theta}$ correspond to the vapour and dry air densities in the far field. Densities on the border $\tilde{\Sigma}_p$ with $t_{ref} = t_n$ are then:

$$\rho_\alpha^{n+\theta} \approx \rho_\alpha^n + \theta \left. \frac{\partial \rho_\alpha}{\partial p_c} \right|_n \Delta p_c^{n+1} + \theta \left. \frac{\partial \rho_\alpha}{\partial p_g} \right|_n \Delta p_g^{n+1} + \theta \left. \frac{\partial \rho_\alpha}{\partial T} \right|_n \Delta T^{n+1} \quad (59)$$

The operators $\tilde{\mathbf{K}}_{\alpha\beta}$ are then modified in order to take into account the convective BC:

$$\tilde{\mathbf{K}}_{\alpha\beta}^n = \tilde{\mathbf{K}}_{\alpha\beta}^n + \theta \mathbf{K}_{\alpha\beta-Conv}^n \quad (60)$$

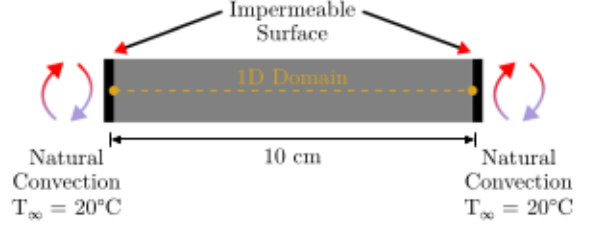


Fig. 3 Geometry and boundary conditions of the simulated case of the UHPC composition following Sciumè et al. [37]

where:

$$\mathbf{K}_{\alpha\beta-Conv}^n = \int_{\tilde{\Sigma}_p} h_g^{n+\theta} \left. \frac{\partial \rho_\alpha}{\partial p_\pi} \right|_n \mathbf{N}^T \mathbf{N} d\Sigma \quad (61)$$

where $\alpha, \beta = c, g, T$ and $\pi, \tau = v, c, g$ accordingly to the considered relationship.

These terms are required to solve the singularity of the operators $\tilde{\mathbf{K}}_{\alpha\beta}$.

The numerical implementation realized in the presented work is based on [46, 57], later enhanced by Sciumè [45]. In this framework, the thermo-hydral numerical model is implemented within a fully coupled monolithic approach in the finite element software FEniCS [58], as proposed in Moreira et al. [50, 59]. We note that the code is available in a GitHub repository at: <https://github.com/ANR-MultiFIRE/THC/>

3 Numerical analysis

In this section, three cases will be investigated using the numerical model proposed. First, a validation of the model with a room temperature test is presented, highlighting the capability of predicting the early age behavior of concrete. This part will serve as validation of the model and its implementation in FEniCS. The reference data is from Sciumè et al. [37] and it was benchmarked against experimental results. Next, the effect of the age of the concrete is considered for the Kalifa results [16], one of the most common experimental results used for benchmarks of numerical simulations of concrete at high temperatures. The analysis of the effect of different curing times on the pressure evolution is also considered. Finally, a benchmark of a mass loss experiment reported by

Composition UHPC

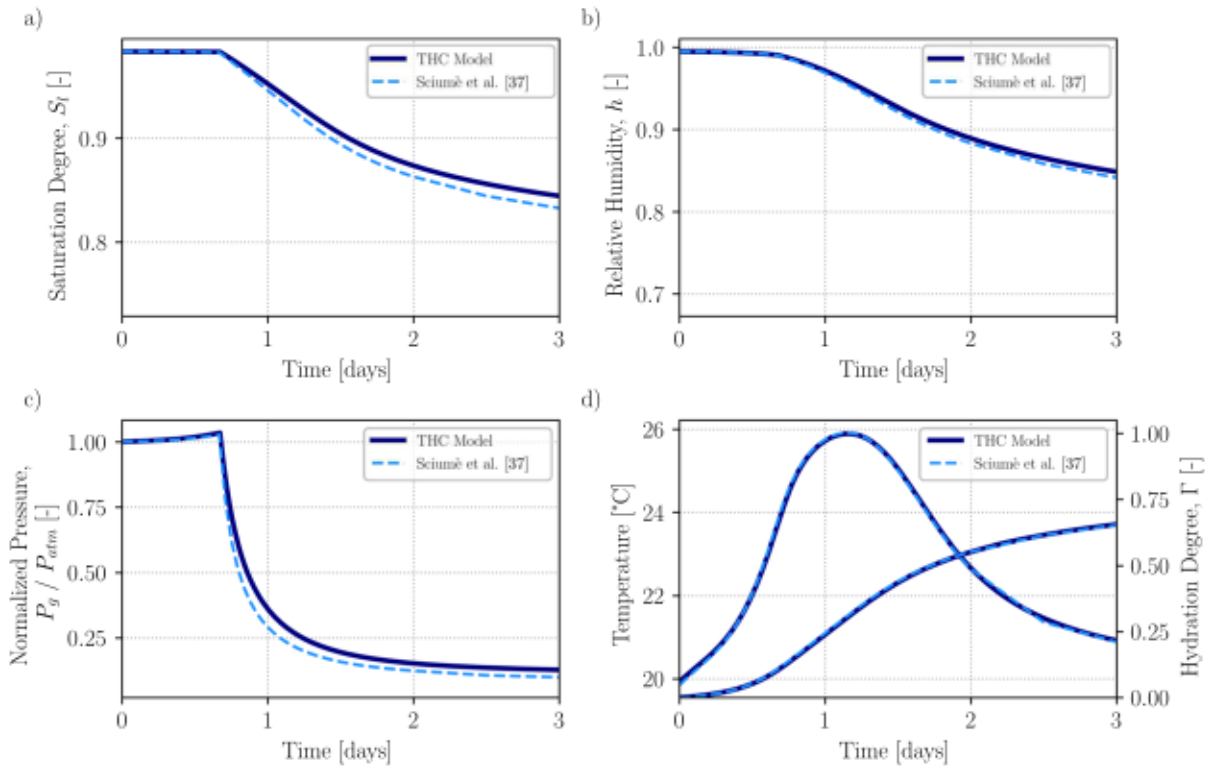
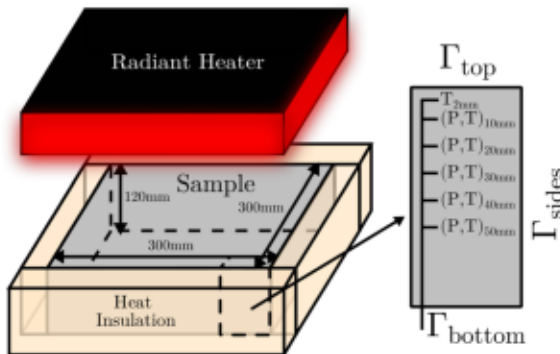


Fig. 4 Validation of the thermo-hydro-chemical (THC) model for a UHPC composition considering **a** saturation degree, **b** relative humidity, **c** normalized pressure and **d** temperature

and hydration degree evolution at room temperature conditions considering the results of Sciumè et al. [37]



Mass Boundary Conditions	Thermal Boundary Conditions
Permeable on Γ_{top}	Heating by thermal radiation and natural convection on Γ_{top} ($T_{heater} = 600^{\circ}C$)
Permeable on Γ_{sides}	Adiabatic on Γ_{sides}
Impermeable on Γ_{bottom}	Cooling by natural convection on Γ_{bottom} ($T_{\infty} = 20^{\circ}C$)

Fig. 5 Geometry and boundary conditions of the simulated case of the M100 high performance concrete following Kalifa et al. [16]

Kanema et al. [38] is proposed to illustrate how the model proposed herein can reproduce such tests by only considering the concrete's composition and the constitutive laws accordingly. The effect of different

aging scenarios is also proposed, highlighting the importance of the concrete history on the measure properties.

3.1 Case I–Validation of room temperature tests

The first analysis aims to validate the THC model, considering the description of the early age behavior of concrete at room temperature. The test represents the curing of concrete in sealed condition, where only heat can be transported on both sides of a 10 cm wide concrete sample through natural convection with a surrounding environment at 20° C and a heat exchange coefficient of 10 W/(m²K), as shown in Figure 3. An ultra-high performance concrete composition (UHPC) is considered: the reader is referenced to [37] for more details.

Figure 4 summarizes the results for the UHPC curing at room temperature. The evolution of the saturation degree, relative humidity and normalized pressure are given in a, b and c. As the cement is hydrated, the free water is consumed and the saturation with liquid water decreases, as well as the relative humidity and the normalized pressure. The thermally activated hydration reaction is exothermic and as it progresses a temperature rise within the sample can be observed, as described by the evolution depicted in Fig. 4d.

Both the model originally proposed in [37] and the current work show similar behavior. The minor difference observed in the late times on the saturation degree, relative humidity and normalized pressure can be related to the different approaches proposed in the different models, such as the monolithic strategy

adopted by the current THC model and the use of the hydration degree as a primary variable.

This comparison validates the possibility of obtaining the curing evolution of concrete at room temperatures by the THC model proposed herein, and the next step is to consider the effect of curing and aging over the high temperature behavior of concrete.

3.2 Case II–Age effect on PTM test results

PTM results are widely used within the study of concrete under fire accidents scenarios. In theory, they can provide the temperature distribution and most importantly the gas pressure during the heating of concrete [16, 29, 60–63]. Such data would enable direct comparison between different concrete under similar conditions [16, 60] or even the effect of different heating protocols [29, 60].

In reality, several challenges hinder broader conclusions to be drawn from such tests over the concrete likelihood to spalling. These issues comprise the large variability of measured gas pressures [30] even on similar concrete compositions, and also the effect that the mere presence of the thermocouples and pressure sensors exert on the concrete microstructure as reported by Dauti et al. [20].

Nonetheless, as one of the most widely used test to validate and calibrate numerical models, the Kalifa results [16] for the M100 high performance concrete will be considered here to first benchmark the capability of modelling the concrete's high

Fig. 6 Comparison of the PTM test results [16] with the thermohygro (TH) and thermo-hygro-chemical (THC) models considering a) temperature and b) gas pressure evolution

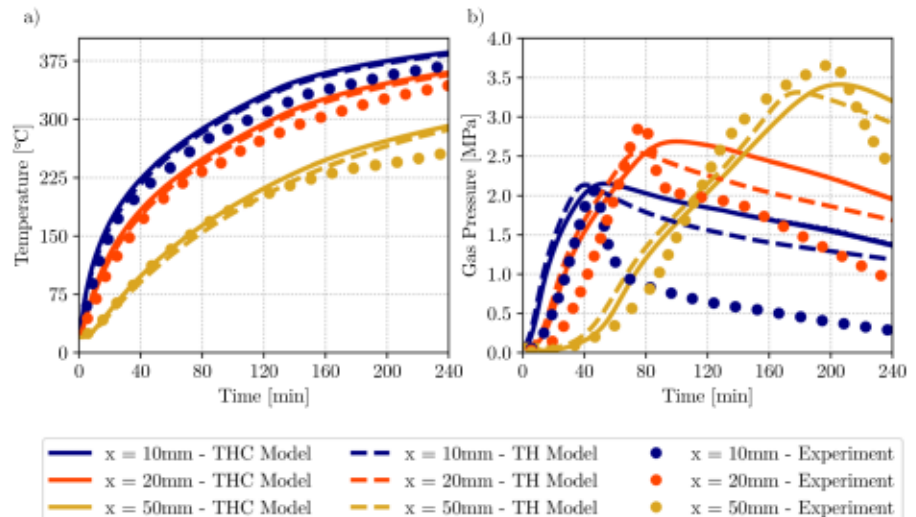


Fig. 7 **a** Temperature, **b** Gas Pressure and **c** Effective Hydration Degree evolution at different positions within the sample over time for samples with different curing durations of 1 day, 15 days, 6 months and 3 years

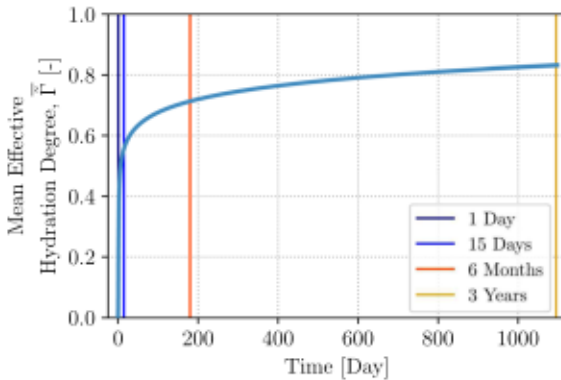
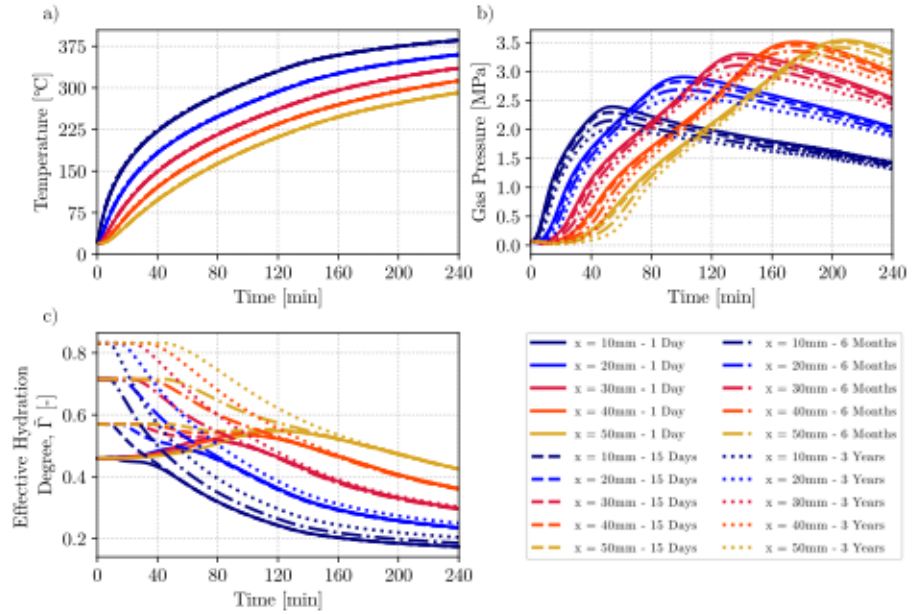


Fig. 8 Evolution of the sample's mean effective hydration degree over time. The colored vertical lines represent each one of the curing scenarios analyzed comprising a duration of 1 day, 15 days, 6 months and 3 years

temperature behavior and, second, to observe the effect of different curing periods on concrete. The setup for the PTM test is described in Figure 5, highlighting the sample geometry and boundary conditions. The radiant heater was at 600°C and the sides were thermally insulated with ceramic blocks [16].

Figure 6 presents the comparison of the current THC results with the implementation described in Moreira et al. of a thermohygro model (TH model) [59] and the experimental values obtained by Kalifa

et al. [16]. It was observed that the temperature evolution described in Fig. 6a predicted by both the TH and THC models are within 2°C–3°C, and are both larger than the values measured in the experimental setup.

In Fig. 6b, the gas pressure evolution can be separated in two distinct stages, the first which is the pressurization and the second which is the gas pressure relief. It can be observed that both the TH and THC results are very similar during such stage, while the peak values and the pressure decrease are larger for the TH model. This can be explained by the effect of the hydration degree over the saturation degree which is proposed in the THC model, following Eq. (31). Still, both models overestimate the pressure increase before reaching the peak, and neither can they reproduce the strong decay of pressure observed experimentally. This is likely related to the formation of cracks [19], which increases the permeability of the regions closer to the hot face and at latter moments, when the sample gets even hotter, the damage increases even more the permeability. As this mechanical damage is not considered in the current model, they do not reproduce this possible behavior that explains the differences between experiment and models.

Figure 7 presents the effect of different curing times on the temperature, gas pressure and on the effective hydration degree. The effect of aging over

the thermal properties are negligible as the thermal evolution is unaltered even when comparing the prediction of a concrete sample after 1 day of casting and after three years, as observed in Fig. 7a. When considering the gas pressure, Fig. 7b, the aging effect is clear, as the pressure observed in older samples is smaller due to the consumption of the free water that once consumed by the hydration reaction will only be released by the hydrates at higher temperatures. The largest difference occurred at the 20 mm between the sample cured for 1 day (solid line in blue) and 3 years (dotted line in blue), which changed the maximum pressure predicted at such position by approximately 10%.

It is important to consider that this overall trend cannot be interpreted as the general behavior of concrete as the current model does not consider the

heterogeneity present at the mesoscale and that much more complex behavior can be seen during the aging of concrete as the water is not uniformly distributed in the concrete. Nonetheless, the current THC model presents an important step towards considering this complexity on the simulations of concrete at high temperatures.

The trend observed in the evolution of the effective hydration degree with time illustrates and explains the difference in the pressure evolution. The longer the curing time, the larger the initial effective hydration degree. It is even possible to observe that for the sample with only a single day of curing (solid line), the hydration reaction actually takes place during the PTM test for the innermost positions (given that this is a thermoactivated reaction), something that cannot

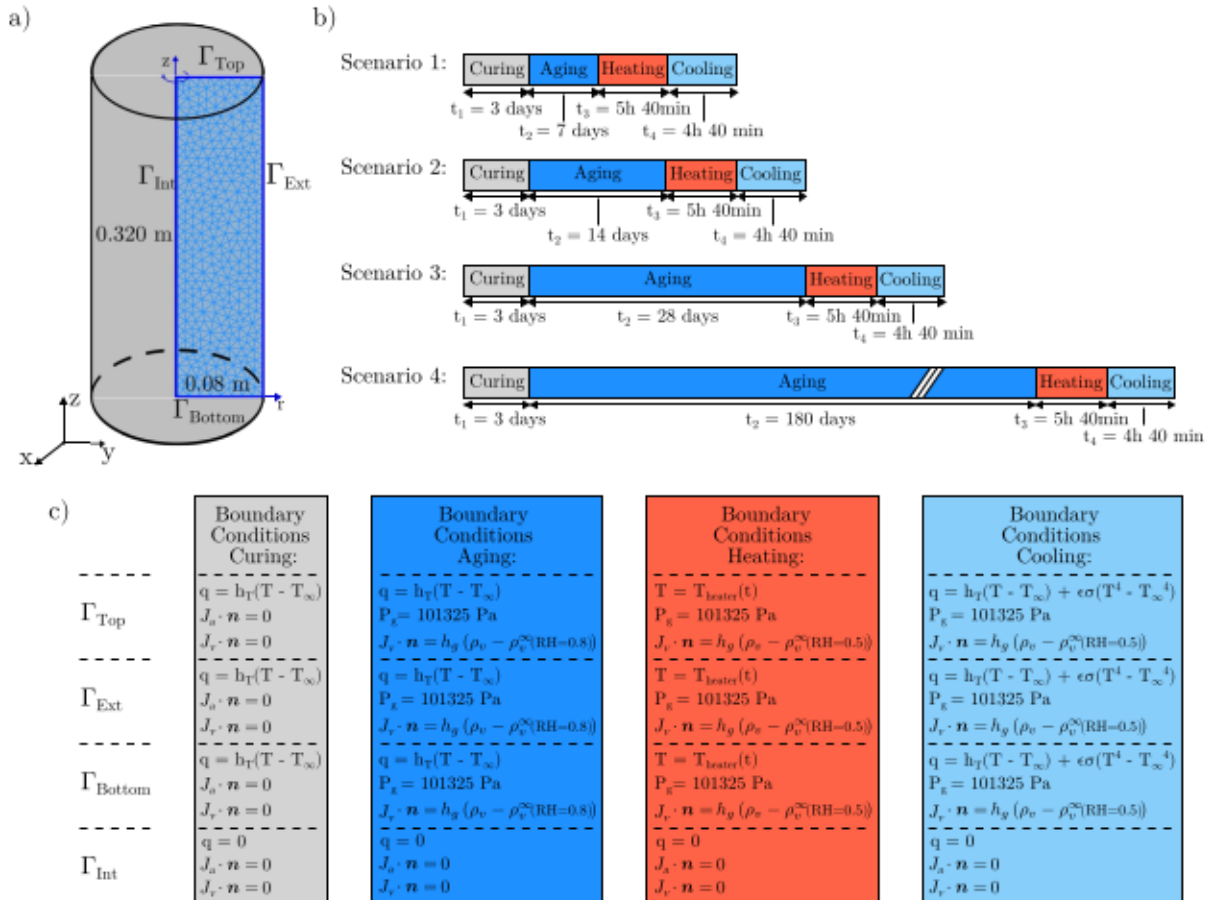
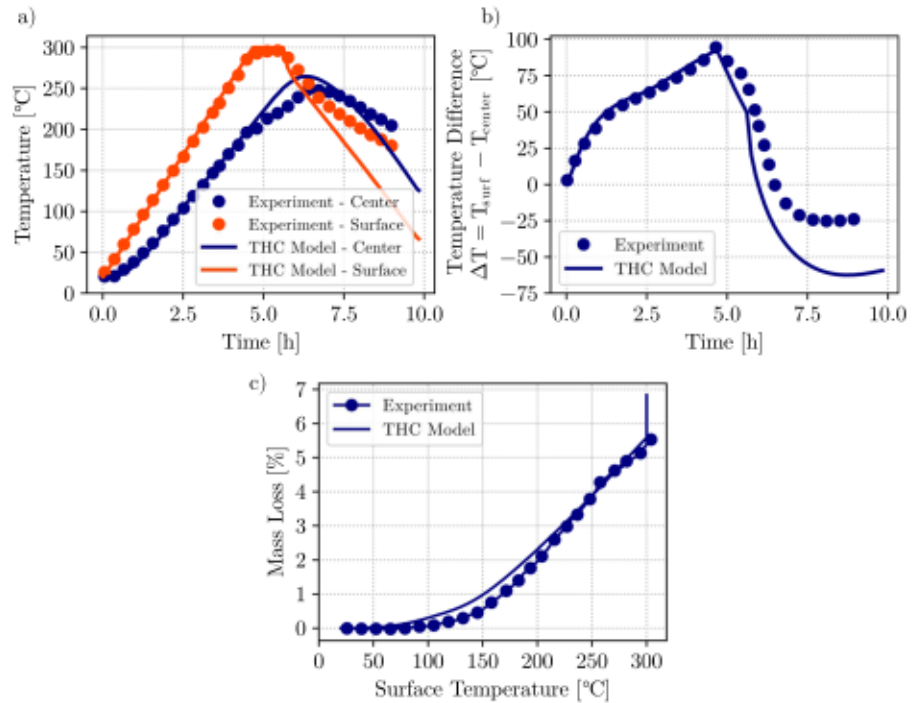


Fig. 9 a Geometry of the Case III numerical simulation, b summary of the different scenarios and c the set of boundary conditions considered for each stage of the simulation

Fig. 10 a) Temperature evolution at the sample's center and surface, b) evolution of temperature difference between surface and center and c) mass loss as a function of the sample temperature



be observed or the samples with longer curing, in which the reactions already started to occur.

In order to assess the overall development of the hydration degree with time, Fig. 8 presents the evolution of the mean of $\bar{\Gamma}$. At the 1-day mark, the hydration reaction did not reach the stable phase evolution, this explains why it was possible to see hydration occurring during the heating stage as seen in Figure 7c. The heating tests at 15 days, 6 months and 3 years occurred at distinct hydration degree stages, thus supporting that the sample's history can indeed affect the dynamics of water removal from concrete.

The next section presents such aspects from another perspective, instead of considering the gas

pressure and temperature evolution, the next case considers the age effect on the mass loss of cylindrical samples based on the test proposed by Kanema et al. [38].

3.3 Case III—Age effect on mass loss experiment

The last case presented comprises both an experimental benchmark based on the mass loss of a concrete specimen and the simulation of different scenarios and their effect on the results. The selection of this test was determined due to the fact that this is a standard test performed in laboratory-scale experiments

Fig. 11 a) Mass loss of samples after 7 days, 14 days, 28 days and 6 months. b) Saturation degree with liquid water distribution at the center line of the sample when the surface temperature is 120° C

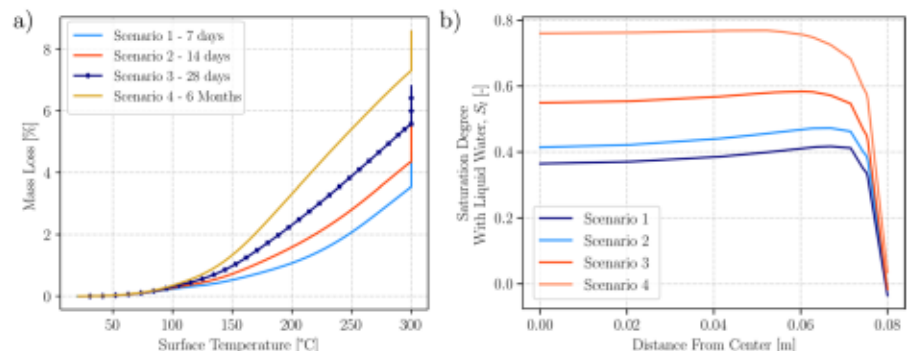
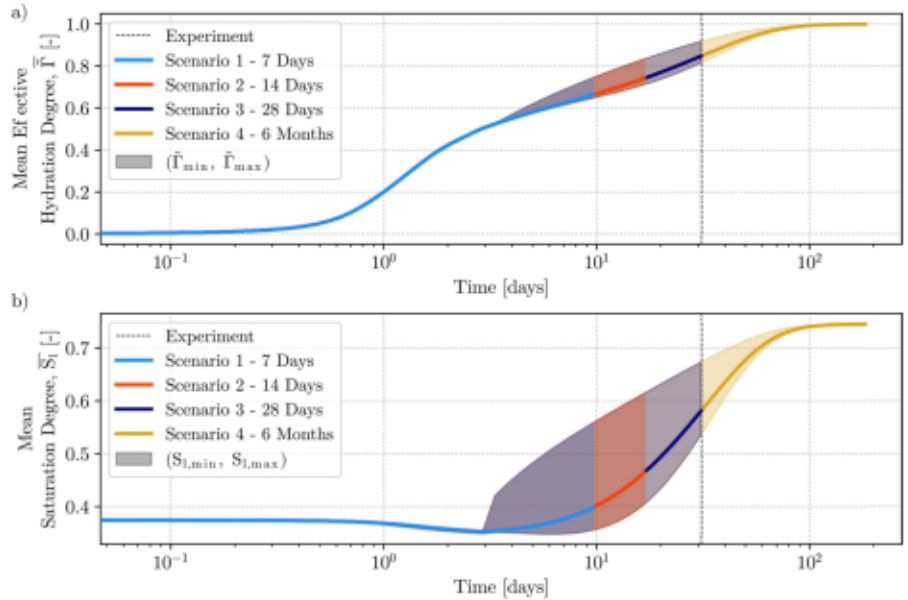


Fig. 12 Evolution of **a** the mean effective hydration degree and **b** mean saturation degree as a function of time. A logarithm scale is used for the timescale, due to the difference of the different scenarios aging duration



[14, 15] comprising tests of cylinders with 16 cm in diameter and 32 cm in height after the 28-day mark. In order to investigate if tests performed at a later or earlier moment would have considerable differences, distinct aging durations were simulated. The geometry studied as well as a summary of the scenarios and the set of boundary conditions at each distinct stage is presented in Fig. 9. A summary of the material properties can be found in Table 2

The sample is described by a 2D axisymmetric unstructured triangular mesh with 688 linear continuous Galerkin elements as described in Fig. 9a. Following the experimental procedure described in [38], the simulation comprises 4 stages, which are first a curing with impermeable boundary conditions, second an aging in an environment with high relative humidity (in the case reported the sample was stored in water) followed by a heating and, finally, a cooling stage. The boundary conditions applied to model each stage are described in Fig. 9c. Four scenarios are presented with different aging durations as described in Fig. 9b, with varying aging durations of 7, 14, 28 and 180 days. The experimental results reported by Kanema et al. were obtained under Scenario 3 and both the tests and the simulation are shown in Fig. 10.

The surface temperature follows the experimental measurements due to the use of the Dirichlet boundary condition and the evolution in the center of the sample follows well the measured values until reaching 200°C , when the calculations start

to overestimate the temperature increase, as shown in Fig. 10a. The cooling also is more intense in the simulation than what is seen on the sample. These observations are also highlighted in Fig. 10b, which describes the temperature difference between surface and sample's center evolution.

The mass loss described in Fig. 10c shows that the THC model captures the overall dynamics of water removal, with the sample drying faster between 75°C and 225°C . Further, adjustments of the constitutive equations used to reproduce the composition might lead to a complete overlap of the results. One feature, however, that is very distinct is the negligible mass loss observed in the experiment during the one-hour plateau, which is not the case in the current model when almost 1% of the mass loss takes place during the temperature hold period at 300°C .

Nonetheless, the model can reproduce the mass loss observed experimentally by only considering the initial formulation of the concrete composition as well as the boundary conditions that the sample was subject to. This highlights how such traditional experiments can be replaced by numerical tests.

To assess the effect of different aging lengths Fig. 11a shows the mass loss of the four different scenarios. From room temperature until reaching 120°C , the mass loss curves are very similar for all the different scenarios. This can be related to the fact that at such temperatures the drying front still did not reach the innermost positions of the sample,

Table 2 Summary of properties of the concrete composition B400 considered for modelling the thermogravimetry tests reported by Kanema et al. [38]

Property	Value/Equation	Reference
Cement Content, c	400 kg/m ³	[38]
Water Content, w	177 kg/m ³	[38]
Aggregates, agg	1789 kg/m ³	[38]
Initial Solid Density, $\rho_{s,0}$	2367 kg/m ³	[38]
Porosity Evolution, $\phi(\Gamma)$	Equation (26)	This work
Chemical Affinity, A_T	Equation (A.1)	[37]*
Relative Humidity Effect on Hydration Rate, β_{RH}	Equation (A.2)	[37]*
Activation Energy of Hydration, E_a	37413 J/mol	[37]*
Enthalpy of Dehydration, H_{dehyd}	58.04 MJ/Kg	[37]*
Specific Heat of Solid, $C_{p,s}(T)$	Equation (A.3)	[38]
Thermal Conductivity Evolution, $\lambda(T)$	Equation (A.4)	[38]
Initial Intrinsic Permeability, K_0	7.5x10 ⁻²⁰ m ²	This work
Intrinsic Permeability Law, $K(I)$	Equation (A.5)	This work
Gas Relative Permeability, $k_{rg}(T, S_i)$	Equation (A.6)	[38]
Liquid Relative Permeability, $k_{rl}(T, S_i)$	Equation (A.7)	[38]
Effective Diffusivity of Vapor in Air, D	Equation (A.8)	[54]
Dehydration Degree, $F(T)$	Equation (18)	[26]
Saturation Degree, $S_i(T, p_c, \Gamma)$	Equation (31)	This work
Saturation Degree Coefficient a_0	32897500 Pa	This work
Saturation Degree Coefficient b	2.11	This work
Initial Water Surface Tension γ_0^w	0.073 N/m ²	[64]
Water Surface Tension $\gamma^w(T)$	Equation (A.11)	[64]
Emissivity, ϵ	0.85	–
Mass Transfer Coefficient, h_g	0.00018 m/s	–
Heat Transfer Coefficient During Curing, h_T	8.3 W/(m ² K)	–
Heat Transfer Coefficient During Cooling, h_T	10 W/(m ² K)	–
Initial Gas Pressure, $P_{g,0}$	101325 Pa	–
Initial Relative Humidity, RH_0	0.9825	–
Initial Temperature T_0	20° C	–
Initial Hydration Degree Γ_0	0	–

*It should be noted that the real hydration dynamic parameters are dependent in the mix-design, and that for quantitative studies data from an adiabatic calorimetry test are needed. In the current work, the data for both Kalifa and Kanema tests were based in the data from Sciumè et al. [37]

where the saturation degree difference of the samples is the largest. This can be seen in Figure 11b.

At higher temperatures, however, it is observed that the final mass loss increased as the duration of the aging was longer because the environment had a higher relative humidity. Such finding can be directly observed on the evolution of the mean effective hydration and saturation degree present in Fig. 12.

It is worth noting that the current composition was completely hydrated ($\bar{\Gamma}$) around the 100-days mark, while the sample that was tested showed an effective hydration degree of approximately 0.85 and was still at an inhomogeneous state, that is, the core still had a smaller hydration degree than

the surfaces. This can be seen from the difference between $\bar{\Gamma}_{min}$ and $\bar{\Gamma}_{max}$.

The evolution of the saturation degree also provides an explanation for the observed mass loss. As the sample starts to cure, the free liquid water is consumed by the hydration reaction, until the sample is exposed to the ambient with larger relative humidity. The first region of linear increase of $S_{l,max}$, is related to the boundary conditions applied as due to numerical issues, the relative humidity of the far field is slowly increased. This increase in liquid water content also finishes around the 100-day mark.

It is noteworthy, however, how the different aging duration can lead to distinct mass loss as

suggested by the model results. This can be an important consideration for both the analysis of the severity of concrete structures with different ages subject to fire, as well as to aid the design of experimental protocols that might better reproduce real cases.

4 Conclusions

Concrete is not an immutable material. Because of the incomplete reactions that take place during curing and which continues throughout its aging history, the hygral state - and as a consequence its own micro-structure - can change considerably during its service time.

The current state of the research on concrete materials provides several experimental results and numerical models that helps to describe the behavior of concrete at high temperatures. With the objective of understanding the critical effect of the age and history of concrete on its spalling behavior, a fully-coupled thermo-hygro-chemical model was proposed here in, based on properties readily available in the literature. This model takes into consideration the effect of both the temperature and relative humidity in the chemical evolution of the concrete properties. The numerical implementation was validated by considering the results of curing simulations at room temperatures as well as comparing the pressure buildup and mass loss observed in experiments.

Besides the benchmarks, a new retention curve law that removes the discontinuity of others' implementations was also proposed. This new constitutive law results in an enhanced numerical stability, which for this strongly non-linear problem prevents problems especially when subjected to severe loading conditions like in a fire or in a nuclear reactor accident (LOCA) [46]. With the ability of simulating the hydration development during the concrete structure aging, multiple scenarios of different aging durations were assessed. It was observed that the peak gas pressure predicted by the model for a freshly cast sample (after one day of curing was 10% higher than what was estimated for a 3 year old sample. When considering a sample subject to a high relative humidity environment during its curing, it was seen that the mass loss could vary by 4.5 wt. %

The current thermo-hygro-chemical (THC) model has a large potential of uncovering important relationships that will enable both the better understanding of the explosive spalling phenomenon and propose new strategies that can reduce the risk of structural failure in fire accidents. This can be especially important when considering massive structures which will only reach their hygral equilibrium after years and that also displays a heterogeneous distribution of the hydrated phase. In future works, the consideration of such effects on real accident scenarios at the structure level will be considered.

Finally, the current study also highlights an important alternative to the debatable although widely adopted strategy of considering incoherent material data from the literature and calibrate the concrete constitutive laws using PTM tests, which can be unreliable. The methodology described herein relies on a limited number of simple characterization tests, thus resulting in a consistent material dataset and a streamlined calibration procedure. Furthermore, in this way, most standard experiments at high temperature could be replaced by numerical analysis, thus allowing to deploy the resources (limited by definition) on innovative tests and not merely characterization experiments.

Acknowledgements This study was financed in part by the Coordenação de Aperfeiçoamento de Pessoal de Nível Superior - Brasil (CAPES) - Finance Code 001 and the Agence National pour la Recherche (ANR) - project ANR-23-CE51-0001. The authors would like to thank the Fundação de Amparo à Pesquisa do Estado de São Paulo - FAPESP (grant numbers: 2021/00251-0 and 2022/12,406-0).

Declarations

Conflict of interest The authors declare that they have no Conflict of interest.

Properties of the B400 concrete composition

$$A_{(\Gamma)} = \frac{A_i + (A_p - A_i) \sin \left[\frac{\pi}{2} \left(1 - \left\langle \frac{\Gamma_p - \Gamma}{\Gamma_p} \right\rangle_+ \right) \right]}{\left[1 + \zeta \left\langle \frac{\Gamma - \Gamma_p}{1 - \Gamma_p} \right\rangle_+ \right]} - \left(\frac{A_p}{1 + \zeta} \right) \left\langle \frac{\Gamma - \Gamma_p}{1 - \Gamma_p} \right\rangle_+ \quad (\text{A.1})$$

where $A_j = 2$, $A_p = 17.5$, $\Gamma_p = 0.13$, and $\zeta = 18$. The operator $\langle \square \rangle_+$ is the positive part operator.

$$\beta_{RH} = (1 + (a_B - a_B \cdot RH)^4)^{-1} \quad (\text{A.2})$$

where $a_B = 5$.

$$c_{ps}(T) = \begin{cases} 915, & \text{if } T \leq 115^\circ\text{C} \\ 915 + \frac{(1000-915)}{85} \cdot (T - 115), & \text{if } 115^\circ\text{C} < T \leq 200^\circ\text{C} \\ 1000 + \frac{(T-200)}{2}, & \text{if } 200^\circ\text{C} < T \leq 400^\circ\text{C} \\ 1105, & \text{if } T > 400^\circ\text{C} \end{cases} \quad (\text{A.3})$$

$$\lambda(T) = \lambda_0 - \left(A_0 - A_1 \frac{T}{A_2} \right) \cdot \frac{T}{A_2} \quad (\text{A.4})$$

where $\lambda_0 = 1.36 \text{ W/(m}^\circ\text{C)}$, $A_0 = 0.136 \text{ W/(m}^\circ\text{C)}$, $A_1 = 0.0057 \text{ W/(m}^\circ\text{C)}$, $A_2 = 100^\circ\text{C}$.

$$K(\bar{\Gamma}) = K_0 \cdot 10^{A_r(1-\bar{\Gamma})} \quad (\text{A.5})$$

where $A_r = 1.25$.

$$k_{rg} = \sqrt{1 - S_f} \left(1 - S_f^{1/A_s} \right)^{2A_s} \quad (\text{A.6})$$

$$k_{rl} = \sqrt{S_f} \left(1 - \left(1 - S_f^{1/A_s} \right)^{A_s} \right)^2 \quad (\text{A.7})$$

where $A_s = 0.6$ for both Eqs. A.6 and A.7.

$$D = f_s \cdot D_{va} \quad (\text{A.8})$$

where f_s and D_{va} is given by Eqs. A.9 and A.10, respectively.

$$\beta_{f_s} = \phi^{4/3} \cdot (1 - S_f)^{10/3} \quad (\text{A.9})$$

$$D_{va} = D_{v,0} \cdot \left(\frac{T}{T_{0,K}} \right)^{A_v} \cdot \left(\frac{P_{g,ref}}{P_g} \right) \quad (\text{A.10})$$

where $D_{v,0} = 2.58e - 5 \text{ m}^2/\text{s}$, $A_v = 1.667$, $T_{0,K} = 273.15\text{K}$, and $P_{g,ref} = 101, 325\text{Pa}$.

$$\gamma(T) = \begin{cases} A_0 \cdot \left(1 - \frac{T}{T_{cr}} \right)^{A_2} \cdot \left[1 - 0.625 \cdot \left(1 - \frac{T}{T_{cr}} \right) \right], & \text{if } T \leq 374.15^\circ\text{C} \\ 0, & \text{if } T > 374.15^\circ\text{C} \end{cases} \quad (\text{A.11})$$

where $A_0 = 0.2358 \text{ J/m}^2$ and $A_2 = 1.256$.

References

- Fillmore DL, Winston PL, Morton SL, Hoffman CR, Van Ausdeln LA, Saegusa T, Shirai K, Hattori T, Sasahara A (2005) The long-term performance of concrete in nuclear applications. ASME Press Vessels Piping Conf 41928:639–648
- Moore J, Tcherner J, Naus D, Bakirov M (2015) Jari Puttonen, and I Moga. Aging management of concrete structures in nuclear power plants, IASMiRT
- V Di Murro, L Pelecanos, K Soga, C Kechavarzi, R F Morton, and L Scibile (2019) Long-term deformation monitoring of cern concrete-lined tunnels using distributed fibre-optic sensing. Geotechnical Engineering Journal of the SEAGS & AGSSEA, 50(1)
- Liu W, Chen J, Luo Y, Chen L, Zhang L, He C, Shi Z, Xu Z, Zhu H, Hu T (2022) Long-term stress monitoring and in-service durability evaluation of a large-span tunnel in squeezing rock. Tunnell Undergr Space Technol 127:10461104611
- Maruyama I, Sasano H, Nishioka Y, Igarashi G (2014) Strength and young's modulus change in concrete due to long-term drying and heating up to 90 c. Cement Concr Res 66:48–63
- Fillmore DL (2004) Literature review of the effects of radiation and temperature on the aging of concrete. Technical report, Idaho National Lab.(INL), Idaho Falls, ID (United States)
- Gallé C, Pin Michel, Ranc G, Rodrigues S (2003) Effect of the heating rate on residual thermo-hydro-mechanical properties of a high-strength concrete in the context of nuclear waste storage (h381). Technical report, International Association for Structural Mechanics in Reactor Technology(IASMiRT)
- Kirkland CJ (2002) The fire in the channel tunnel. Tunnell undergr Space Technol 17(2):129–132
- Bazant ZP (1976) Instability, ductility, and size effect in strain-softening concrete. J Eng Mech Div 102(2):331–344
- Jansson R (2013) Fire spalling of concrete: theoretical and experimental studies. PhD thesis, KTH Royal Institute of Technology
- Dal Pont S, Ehrlicher A (2004) Numerical and experimental analysis of chemical dehydration, heat and mass transfers in a concrete hollow cylinder submitted to high temperatures. Int J Heat Mass Transf 47(1):135–147
- Moreira MH, Dal Pont S, Ausas R, Luz AP, Cunha T, Parr C, Pandolfelli VC (2021) Main trends on the simulation of the drying of refractory castables-review. Ceram Int 47(20):28086–28105
- Pham DT, Pinoteau N, Yang M, de Buhan P, Pimienta P, Mège R (2021) Full-scale fire test on a high-rise RC wall. Eng Struct 227:111435
- Pliya P, Beaucour AL, Noumowé A (2011) Contribution of cocktail of polypropylene and steel fibres in improving the behaviour of high strength concrete subjected to high temperature. Construct Build Mater 25(4):1926–1934
- Noumowe A, de Morais MVG, Kanema M, Gallias JL, Cabrillac R (2006) Heat and mass transfers in a heated

- concrete element: 20 to 600° c. In: Fluids Engineering Division Summer Meeting 47500:1007–1013
16. Kalifa P, Menneteau FD, Quenard D (2000) Spalling and pore pressure in HPC at high temperatures. *Cement Concr Res* 30(12):1915–1927
 17. Dal Pont S, Colina H, Dupas A, Ehrlicher A (2005) An experimental relationship between complete liquid saturation and violent damage in concrete submitted to high temperature. *Magazine Concr Res* 57(8):455–461
 18. Bangi MR, Horiguchi T (2011) Pore pressure development in hybrid fibre-reinforced high strength concrete at elevated temperatures. *Cement Concr Res* 41(11):1150–1156
 19. Dauti D (2018) A combined experimental and numerical approach to spalling of high performance concrete due to fire. PhD thesis, Université Grenoble Alpes
 20. Dauti D, Tengattini A, Dal Pont S, Toropovs N, Briffaut M, Weber B (2020) Some observations on testing conditions of high-temperature experiments on concrete: an insight from neutron tomography. *Transp Porous Media* 132:299–310
 21. Dauti D, Tengattini A, Dal Pont S, Toropovs N, Briffaut M, Weber B (2018) Analysis of moisture migration in concrete at high temperature through in-situ neutron tomography. *Cement Concr Res* 111:41–55
 22. Sleiman H, Tengattini A, Briffaut M, Huet B, Dal Pont S (2021) Simultaneous x-ray and neutron 4d tomographic study of drying-driven hydro-mechanical behavior of cement-based materials at moderate temperatures. *Cement Concr Res* 147:106503
 23. Moreira MH, Dal Pont S, Tengattini A, Luz AP, Pandolfelli VC (2022) Experimental proof of moisture clog through neutron tomography in a porous medium under truly one-directional drying. *J Am Ceram Soc* 105(5):3534–3543
 24. Pimienta P, Jansson McNamee R, Mindeguia J-C (2019) Physical properties and Behaviour of high-Performance Concrete at high Temperature - RILEM State-of-the-Art Reports. Springer
 25. Bažant ZP, Thonguthai W (1978) Pore pressure and drying of concrete at high temperature. *J Eng Mech-ASCE* 104(5):1059–1079
 26. Pesavento F (2000) Nonlinear modelling of concrete as a multiphase material in high temperature conditions. PhD thesis, Università degli Studi di Padova
 27. Gawin D, Pesavento F, Schrefler BA (2011) What physical phenomena can be neglected when modelling concrete at high temperature? a comparative study. part 1: Physical phenomena and mathematical model. *Int J Solids Struct* 48(13):1927–1944
 28. Davie CT, Pearce CJ, Bičanić N (2006) Coupled heat and moisture transport in concrete at elevated temperatures—effects of capillary pressure and adsorbed water. *Numer Heat Transf, Part A: Appl* 49(8):733–763
 29. Fey KG, Riehl I, Wulf R, Gross U (2016) Experimental and numerical investigation of the first heat-up of refractory concrete. *Int J Therm Sci* 100:108–125
 30. Dauti D, Tengattini A, Dal Pont S, Toropovs N, Briffaut M, Weber B (2018) Analysis of moisture migration in concrete at high temperature through in-situ neutron tomography. *Cement Concr Res* 111:41–55
 31. Jkdrzejewska A, Benboudjema F, Lacarrière L, Azenha M, Schlicke D, Dal Pont S, Delaplace A, Granja J, Hajkova K, Joachim Heinrich P (2018) Cost tu1404 benchmark on macroscopic modelling of concrete and concrete structures at early age: proof-of-concept stage. *Construct Build Mater* 174:173–189
 32. You Weijie, Zhang Fengping, Huang Yue, Gao Mi, Wen Chengqian, Yang Guotao (2020) A coupled hygro-thermo-mechanical model for the evolution of saturation in early-age concrete. *Int J Heat Mass Transf* 156:119817
 33. You Weijie, Liu Xiaoyang, Shang Huaishuai, Yang Guotao (2021) Evolution of temperature, humidity and deformation in early-age cement-based materials based on a multi-field model. *Construct Build Mater* 290:123277
 34. Liang Minfei, Chang Ze, Shan He Yu, Chen Yidong Gan, Schlangen Erik, Šavija Branko (2022) Predicting early-age stress evolution in restrained concrete by thermo-chemo-mechanical model and active ensemble learning. *Computer-Aided Civil Infrastruct Eng* 37(14):1809–1833
 35. Silvio Prskalo, Michael Helmut Grferer, and Martin Schanz (2023) Multiphase model of early stage hydration in concrete using the theory of porous media. PAMM, page e202300220
 36. Powers TC, Brownard TL (1946) Studies of the physical properties of hardened Portland cement paste. *Bull 22, Res Lab Portland Cement Assoc* 43(9):101–132
 37. Sciumè G (2013) Thermo-hygro-chemo-mechanical model of concrete at early ages and its extension to tumor growth numerical analysis. PhD thesis, Université degli studi (Padoue, Italie)
 38. Kanema M, De Moraes MVG, Noumowe A, Gallias JL, Cabrillac R (2007) Experimental and numerical studies of thermo-hydrous transfers in concrete exposed to high temperature. *Heat Mass Transf* 44:149–164
 39. Hassanizadeh M, Gray WG (1979) General conservation equations for multi-phasesystems: 1. averaging procedure. *Adv Water Resour* 2:131–144
 40. Hassanizadeh M, Gray WG (1979) General conservation equations for multi-phase systems: 2. mass, momenta, energy, and entropy equations. *Adv Water Resour* 2:191–203
 41. Hassanizadeh M, Gray WG (1980) General conservation equations for multi-phase systems: 3. constitutive theory for porous media flow. *Adv Water Resour* 3(1):25–40
 42. Lewis R, Schrefler BA (1998) The Finite Element Method in the Static and Dynamic Deformation and Consolidation of Porous Media. John Wiley
 43. Gawin D, Majorana CE, Schrefler BA (1999) Numerical analysis of hygro-thermal behaviour and damage of concrete at high temperature. *Mech Cohesive-frictional Mater* 4(1):37–74
 44. Dalton Laura E, LaManna Jacob M, Jones Scott, Pour-Ghaz Mohammad (2022) Does it influence moisture transport in concrete? *Transp Porous Media* 144(3):623–639
 45. Sciumè G, Benboudjema F, De Sa C, Pesavento F, Birtaud Y (2013) A multiphysics model for concrete at early age applied to repairs problems. *Eng Struct* 57:374–387
 46. Dal Pont S, Durand S, Schrefler BA (2007) A multiphase thermo-hydro-mechanical model for concrete

- at high temperatures-finite element implementation and validation under LOCA load. *Nuclear Eng Design* 237(22):2137–2150
47. Meftah F, Dal Pont S, Schrefler BA (2012) A three-dimensional staggered finite element approach for random parametric modeling of thermo-hygral coupled phenomena in porous media. *Int J Numer Anal Methods Geomech* 36(5):574–596
 48. Pasquero D (2004) Contribution à l'étude de la déshydratation dans les pâtes de ciment soumise à haute température. PhD thesis, ENPC
 49. Mills RH (1966) Factors influencing cessation of hydration in water cured cement pastes. Highway Research Board Special Report, pages 406–424
 50. Moreira MH, Ausas R, Dal Pont S, Pelissari P, Luz AP, Pandolfelli VC (2021) Towards a single-phase mixed formulation of refractory castables and structural concrete at high temperatures. *Int J Heat Mass Transf* 171:121064
 51. Baroghel-Bouny V, Mainguy M, Lassabatere T, Coussy O (1999) Characterization and identification of equilibrium and transfer moisture properties for ordinary and high-performance cementitious materials. *Cement Concr Res* 29(8):1225–1238
 52. Drouet E, Poyet S, Torrenti J-M (2015) Temperature influence on water transport in hardened cement pastes. *Cement Concr Res* 76:37–50
 53. Davie CT, Pearce CJ, Kukla K, Bićanić N (2018) Modelling of transport processes in concrete exposed to elevated temperatures—an alternative formulation for sorption isotherms. *Cement Concr Res* 106:144–154
 54. Dauti D, Dal Pont S, Weber B, Briffaut M, Toropovs N, Wyrzykowski M, Sciumé G (2018) Modeling concrete exposed to high temperature: impact of dehydration and retention curves on moisture migration. *Int J Numer Anal Methods Geomech* 42(13):1516–1530
 55. Gawin D, Pesavento F, Schrefler BA (2011) What physical phenomena can be neglected when modelling concrete at high temperature? A comparative study. Part 2: Comparison between models. *Int J Solids Struct* 48(13):1945–1961
 56. Lewis RW, Schrefler BA (1998) The finite element method in the static and dynamic deformation and consolidation of porous media. John Wiley and Sons
 57. Dal Pont S, Meftah F, Schrefler BA (2011) Modeling concrete under severe conditions as a multiphase material. *Nuclear Eng Design* 241(3):562–572
 58. Martin S, Blechta J, Hake J, Johansson A, Kehlet B, Logg A, Richardson C, Ring J, Rognes M, and Wells GN (2015) The FEniCS Project version 1.5. *Archive of Numerical Software*, 3(100)
 59. Moreira MH, Dal Pont S, Ausas R, Cunha TM, Luz AP, Pandolfelli VC (2021) Direct comparison of multi and single-phase models depicting the drying process of refractory castables. *Open Ceram* 6:100111
 60. Mindeguia J-C, Pimienta PP, Noumowé A, Kanema M (2010) Temperature, pore pressure and mass variation of concrete subjected to high temperature-experimental and numerical discussion on spalling risk. *Cement Concr Res* 40(3):477–487
 61. Felicetti R, Lo Monte F, Pimienta P (2017) A new test method to study the influence of pore pressure on fracture behaviour of concrete during heating. *Cement Concr Res* 94:13–23
 62. Choe G, Kim G, Yoon M, Hwang E, Nam J, Guncunski N (2019) Effect of moisture migration and water vapor pressure build-up with the heating rate on concrete spalling type. *Cement Concr Res* 116:1–10
 63. Luz AP, Moreira MH, Braulio MAL, Parr C, Pandolfelli VC (2021) Drying behavior of dense refractory ceramic castables. Part 1-general aspects and experimental techniques used to assess water removal. *Ceram Int* 47(16):22246–22268
 64. Cooper JR, Dooley RB (1993) The international association for the properties of water and steam. Proceedings of the International Association for the Properties of Water and Steam (IAPWS)

Publisher's Note Springer Nature remains neutral with regard to jurisdictional claims in published maps and institutional affiliations.

Springer Nature or its licensor (e.g. a society or other partner) holds exclusive rights to this article under a publishing agreement with the author(s) or other rightsholder(s); author self-archiving of the accepted manuscript version of this article is solely governed by the terms of such publishing agreement and applicable law.